# Assessing the Effects of Langmuir Turbulence on the Entrainment Buoyancy Flux in the Ocean Surface Boundary Layer

QING LI AND BAYLOR FOX-KEMPER

*Department of Earth, Environmental and Planetary Sciences, Brown University, Providence, Rhode Island*

(Manuscript received 25 April 2017, in final form 24 September 2017)

ABSTRACT

Large-eddy simulations (LESs) with various constant wind, wave, and surface destabilizing surface buoyancy flux forcing are conducted, with a focus on assessing the impact of Langmuir turbulence on the entrainment buoyancy flux at the base of the ocean surface boundary layer. An estimate of the entrainment buoyancy flux scaling is made to best fit the LES results. The presence of Stokes drift forcing and the resulting Langmuir turbulence enhances the entrainment rate significantly under weak surface destabilizing buoyancy flux conditions, that is, weakly convective turbulence. In contrast, Langmuir turbulence effects are moderate when convective turbulence is dominant and appear to be additive rather than multiplicative to the convection-induced mixing. The parameterized unresolved velocity scale in the *K*-profile parameterization (KPP) is modified to adhere to the new scaling law of the entrainment buoyancy flux and account for the effects of Langmuir turbulence. This modification is targeted on common situations in a climate model where either Langmuir turbulence or convection is important and may overestimate the entrainment when both are weak. Nevertheless, the modified KPP is tested in a global climate model and generally outperforms those tested in previous studies. Improvements in the simulated mixed layer depth are found, especially in the Southern Ocean in austral summer.

## 1. Introduction

The entrainment of dense water from below the ocean surface boundary layer (OSBL) directly controls the deepening and properties of this layer and affects the exchange of heat, momentum, and tracer gases between the atmosphere, the surface ocean, and the deep ocean. Various factors may affect the rate of entrainment, or the entrainment buoyancy flux, $\overline{w'b'}_e$. Two dominant factors providing energy required for entrainment are the destabilizing surface buoyancy flux $B_0$[1] and shear instability localized at the base of the OSBL (Niiler and Kraus 1977; Price et al. 1986). The former controls $\overline{w'b'}_e$ in the convective turbulence regime, commonly with a simple rule of $\overline{w'b'}_e = -0.2B_0$ (e.g., Tennekes 1973; Moeng and Sullivan 1994). The latter is usually associated with inertial oscillations of the surface current and dominates under resonant wind-driven mixing (Large and Crawford 1995; Crawford and Large 1996; Skyllingstad et al. 2000). When both effects exist, a proportionality is commonly assumed by introducing a new velocity scale $w_x$ as a combination of the convective velocity scale $w^* \equiv (B_0 h_b)^{1/3}$ ($h_b$ the boundary layer depth) and the water-side friction velocity $u^* \equiv (\tau/\rho_0)^{1/2}$ ($\tau$ the surface wind stress and $\rho_o$ the water density), that is, $\overline{w'b'}_e = -0.2 w_x^3/h_b$ (Moeng and Sullivan 1994; Large et al. 1994).

In the presence of surface gravity waves, the Stokes drift (see Webb and Fox-Kemper 2011, 2015, and references therein) provides another source of turbulent kinetic energy (TKE) through the vortex force and modified pressure (Craik and Leibovich 1976), or more cleanly the Stokes shear force (Suzuki and Fox-Kemper 2016), converting wave energy to TKE. Evidence of enhanced vertical mixing within OSBL in the presence of Langmuir turbulence, as suggested by the enhanced vertical turbulent velocity variance $\overline{w'^2}$, has been found in observations under a variety of conditions (D'Asaro 2001; Tseng and D'Asaro 2004; D'Asaro 2014) and large-eddy simulation (LES) studies (Skyllingstad and Denbo 1995; McWilliams et al. 1997; Li et al. 2005;

---

[1] Here the surface buoyancy flux is defined to be positive for an upward, destabilizing flux, associated with ocean surface cooling or evaporation.

*Corresponding author*: Qing Li, qing_li_1@brown.edu

DOI: 10.1175/JPO-D-17-0085.1

Polton et al. 2005; Harcourt and D'Asaro 2008; Grant and Belcher 2009; Van Roekel et al. 2012), although some observations suggest that the direct impact of Langmuir turbulence may be confined within the upper half of the mixed layer (Weller and Price 1988; Thorpe et al. 2003). In addition, Langmuir-enhanced $\overline{w'^2}$ is also supported by the rapid distortion theory (RDT) calculations (Teixeira and Belcher 2002, 2010; Teixeira 2011). Though not yet supported by direct observations, enhanced $\overline{w'b'}_e$ in the presence of Langmuir turbulence is reported in several LES studies (e.g., McWilliams et al. 1997; Sullivan et al. 2007; Grant and Belcher 2009; McWilliams et al. 2014). The importance of Langmuir turbulence on entrainment is also suggested by a comparison of LES and observations of the upper-ocean response to a wind event with rapid mixed layer deepening, in which consistencies between LES and observations are found only when the effects of Langmuir turbulence are included in the model (Kukulka et al. 2009). Enhanced shear instabilities beneath downwelling regions of Langmuir cells may be a mechanism for thermocline erosion (Li and Garrett 1997; Smith 1998; Kukulka et al. 2010).

Generally, in the presence of Langmuir turbulence, more TKE is expected to be available near the base of the OSBL for entraining denser water into the mixed layer from below, as a result of both the additional Stokes-shear-induced TKE production and the more efficient downward TKE transport promoted by enhanced vertical mixing. Without explicitly accounting for this effect, boundary layer turbulence models, such as the $K$-profile parameterization (KPP; Large et al. 1994), which might have implicitly incorporated some effects of Langmuir turbulence by tuning the parameters to ocean observations (Reichl et al. 2016, hereinafter RW16), tend to misrepresent the entrainment under varying wave conditions and result in biases in the boundary layer depth. The goal of this paper is to investigate the impacts of Langmuir turbulence on $\overline{w'b'}_e$ quantitatively and to explore possibilities to explicitly incorporate these impacts into a boundary layer model. While results using a modified version of KPP will be evaluated, the impacts are quantified more broadly first, so they may be incorporated into a variety of boundary layer turbulence schemes.

Quantifying the scaling of Langmuir-turbulence-enhanced $\overline{w'b'}_e$ is not as easy as estimating other metrics because of the small magnitude of $\overline{w'b'}_e$ in the TKE budget as a whole. The $\overline{w'b'}_e$ term is a small residual of TKE production, transport, and dissipation, and it tends to result from intermittent events with large variability. To our knowledge, only a few LES studies of Langmuir turbulence have reported directly on the scaling for $\overline{w'b'}_e$. Those that do suggest that the Langmuir-turbulence-enhanced $\overline{w'b'}_e$ scales with $\sim \mathrm{La}_t^{-2}$ (Grant and Belcher 2009; McWilliams et al. 2014), where $\mathrm{La}_t$ is the turbulent Langmuir number (McWilliams et al. 1997). On the other hand, a study that indirectly estimates the entrainment through optimizing the agreement between KPP and LES results of mixing layer depth evolution and surface cooling under tropical cyclone conditions follows a scaling of $\sim \mathrm{La}_{\mathrm{SL,proj}}^{-1/2}$ (RW16), where $\mathrm{La}_{\mathrm{SL,proj}}$ is the surface-layer-projected turbulent Langmuir number (Harcourt and D'Asaro 2008; Van Roekel et al. 2012).

This study focuses on many versions of a scenario in which an initial mixed layer is continuously deepening due to entrainment, where a quasi-equilibrium state is reached under constant destabilizing surface buoyancy flux, wind, and wave forcing. This scenario resembles that of Fig. 2 of Belcher et al. (2012). The structure of the OSBL is illustrated in a schematic in Fig. 1a, with profiles of normalized stratification $N^2$, buoyancy flux $\overline{w'b'}$, and dissipation $\varepsilon$ overlaid on each other. The mean boundary layer depth $h_b$ is defined as the depth where $N^2$ reaches its maximum, corresponding to a barrier where the turbulent motions are suppressed by converting TKE to potential energy. Note that the location of the drop in turbulence dissipation rate agrees roughly with the location of maximum $N^2$ in Fig. 1a, but the latter stratification-based definition was used because it was found to be more robust here. In the quasi-equilibrium mean state, the OSBL consists of two stacked layers: a mixed layer and an entrainment layer. In the mixed layer, buoyancy is nearly uniformly distributed, and $\overline{w'b'}$ is linear with depth matching a surface value set by $B_0$ and $\overline{w'b'}_e$. The mixed layer depth $h_m$ is approximated by the entrainment depth, where $\overline{w'b'}$ reaches its minimum (Grant and Belcher 2009). The entrainment buoyancy flux is therefore defined as $\overline{w'b'}_e \equiv \min(\overline{w'b'}) = \overline{w'b'}|_{z=-h_m}$. The entrainment layer is a layer below the mixed layer where active entrainment of denser water from the higher stratification below the OSBL occurs. This entrainment layer should be distinguished from the stratified shear layer described in Grant and Belcher (2011), in which case the thickness of the stratified shear layer is continuously deepening due to the lack of Earth's rotation while the mixed layer depth remains constant. In the case here, the thickness of the entrainment layer is approximated by the difference between $h_b$ and $h_m$, and with rotation of the Earth it tends to occupy a constant portion of the OSBL. Note that the actual entrainment layer might be thicker as instantaneous entrainment may occur above $z = -h_m$ as well as below $z = -h_b$.

There are other definitions of the mixed layer depth that are more convenient observationally, for example, using a density threshold (de Boyer Montégut et al. 2004), as well as the boundary layer depth, for example,

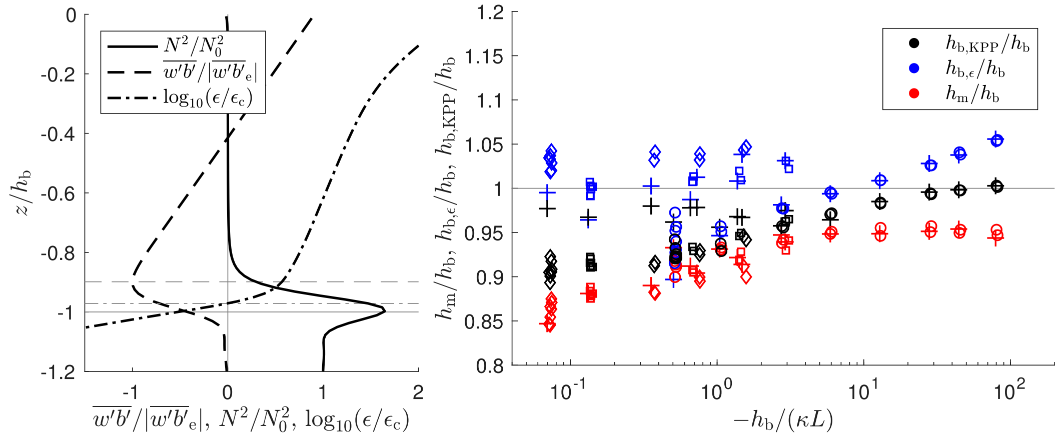

(a) (b)

FIG. 1. (a) Schematic of typical structure of the boundary layer of interest in this study, showing the vertical profiles of $N^2/N_0^2$, $\overline{w'b'}/|\overline{w'b'}_e|$, and $\log_{10}(\varepsilon/\varepsilon_c)$, with $N_0^2$ the stratification below the boundary layer, $|\overline{w'b'}_e|$ the magnitude of the entrainment buoyancy flux, and $\varepsilon_c = 10^{-9}\,\mathrm{m^2\,s^{-3}}$ the dissipation threshold commonly used to define the boundary layer depth. Light lines indicate the mixed layer depth $h_m$ (minimum $\overline{w'b'}$, dashed), depth where $\varepsilon$ hits the threshold ($h_{b,\varepsilon}$, dashed–dotted), and boundary layer depth $h_b$ (maximum $N^2$, solid). (b) The ratios $h_{b,\mathrm{KPP}}/h_b$ (black), $h_{b,\varepsilon}/h_b$ (blue), and $h_m/h_b$ (red) for all simulations in this study, where $h_{b,\mathrm{KPP}}$ is the boundary layer depth diagnosed from KPP. Here the no-Langmuir cases are marked by plus signs, and the Langmuir cases with 5, 8, and $10\,\mathrm{m\,s^{-1}}$ surface wind are marked by circles, squares, and diamonds, respectively.

using a dissipation criterion (see more discussion in Sutherland et al. 2014). However, in simulations the minimum buoyancy flux and maximum stratification criteria are convenient and consistently describe the structure of the OSBL in LES and allow for a precise definition of the entrainment layer and entrainment rate. It should be noted here that when a direct comparison is made between the simulated mixed layer depth and the observations, as will be detailed in section 6, consistent definitions are adopted between the model and observations.

Red symbols in Fig. 1b show the ratio $h_m/h_b$ versus the dimensionless parameter $-h_b/(\kappa L)$, which characterizes the relative importance of convective turbulence versus shear turbulence [$L \equiv -u^{*3}/(\kappa B_0)$ is the Monin–Obukhov length, with $\kappa = 0.4$ the von Kármán constant], for all the simulations in this study (detailed in section 2). Overlaid are the ratios of boundary layer depth defined by the dissipation criterion (with a critical dissipation $\varepsilon_c = 10^{-9}\,\mathrm{m^2\,s^{-3}}$, blue symbols) and diagnosed from a bulk Richardson number criterion as in KPP [see (22) in section 5, black symbols], respectively, to $h_b$. The first thing to notice is that the ratio $h_m/h_b$ approaches a constant (~0.95) as convective turbulence becomes dominating. In the shear turbulence regime, this ratio is smaller, and considerable scatter due to the presence of Langmuir turbulence exists. Figure 1b suggests the existence of significant differences in the structure of the OSBL and presumably also the mechanisms that drive the entrainment under different forcing regimes. The distinguished boundary layer depth given by different definitions confirm this transition of boundary layer structure from shear dominating to convection dominating.

Note that the boundary layer depth diagnosed from KPP seems to be consistent with $h_b$ when convective turbulence dominates. General consistency is also found when wind-driven shear turbulence dominates, without Langmuir turbulence (black plus signs). In the presence of Langmuir turbulence (black empty symbols), the boundary layer depth is significantly underestimated. Accounting for the Stokes shear in the bulk Richardson number by using the Lagrangian velocity in KPP (Haney et al. 2015) alleviates the problem, but significant shallow biases still exist (not shown). One direct application of the new scaling laws developed here for $\overline{w'b'}_e$ in accounting for the entrainment of Langmuir turbulence is improvement of the diagnosed boundary layer depth in KPP (section 5).

The remainder of this paper is organized as follows. In section 2, the LES model and the setup of simulations are introduced. The turbulence statistics and comparison with previous studies are presented in section 3. Scaling of $\overline{w'b'}_e$ to account for the effects of Langmuir turbulence is proposed in section 4. Modifications to KPP based on the newly proposed scaling are presented in section 5, and the effects of the new scaling on the simulated mixed layer depth in a climate model are presented in section 6. This paper ends with the main conclusions in section 7, a brief discussion in section 8, and some appendixes.

## 2. Method

### a. Model description and basic setup

The LES model used in this study was originally developed at NCAR by Moeng (1984) and adapted for ocean applications by McWilliams et al. (1997) to solve the wave-averaged or Craik–Leibovich equations (Craik and Leibovich 1976; Leibovich 1980). The same model with corresponding modifications was used in studies on Langmuir turbulence in pure wind seas (Harcourt and D'Asaro 2008), in misaligned wind and waves (Van Roekel et al. 2012), in swell (McWilliams et al. 2014), under tropical cyclone conditions (RW16), and to investigate the interactions between the surface waves and submesoscale instabilities and frontogenesis (Hamlington et al. 2014; Haney et al. 2015; Suzuki et al. 2016) as well as their impact on the ocean tracer transport (Smith et al. 2016).

In this study, simulations with various wind, wave, and destabilizing surface buoyancy forcing have been carried out to investigate the dependence of $\overline{w'b'}_e$ in the OSBL on the external forcing. Most of these simulations also appear in B. G. Reichl et al. (2017, unpublished manuscript), so while the parameterization approaches differ, they agree with the same set of LES. Details of the parameters are described in the next section. The basic setup of all the simulations is summarized here.

All the simulations are initialized from rest, except for some small random perturbations in velocity within the top few meters to aid the development of turbulence. The initial stratification is neutral in the upper 42 m and stable below ($N = 4.4 \times 10^{-3}\,\mathrm{s}^{-1}$). Temperature is the only active tracer affecting the buoyancy, with a thermal expansion coefficient, $\alpha = 2 \times 10^{-4}\,\mathrm{K}^{-1}$. Therefore, a positive destabilizing surface buoyancy flux is equivalent to surface cooling. The surface buoyancy flux is applied at the first vertical grid cell. Penetrating solar radiation and effects from freshwater fluxes are not considered here.

The domain size is 320 m × 320 m × 163.84 m in the $x$, $y$, $z$ direction, with 256 × 256 × 256 computational cells. This corresponds to a horizontal resolution of $dx = dy = 1.25$ m and a vertical resolution of $dz = 0.64$ m. Doubling the horizontal and vertical resolution appears to slightly decrease the magnitude of $\overline{w'b'}_e$, but the differences are well within the uncertainties described below. A radiation condition for outward propagation only is applied at the lower boundary of the domain. At the end of the simulations, $h_b$ ranges from ~47 to ~76 m, far from the lower boundary of the domain and ≥5 m deeper than the initially neutrally stratified layer. The possible impact of the domain boundary and initial conditions on $\overline{w'b'}_e$ should be small.

The rotation is uniform, with a Coriolis parameter of $f = 1.028 \times 10^{-4}\,\mathrm{s}^{-1}$ (45°N). This corresponds to an inertial oscillation period of about 17 h. To minimize the effect of inertial oscillation due to the sudden onset of wind forcing at the beginning, the integration time for each simulation is chosen so that, after spinup (about 8 h), at least one inertial oscillation period of data is available for time average. The history of the horizontally averaged turbulence statistics is saved every 30 time steps and the time average is performed over the last inertial oscillation period. The integration time step varies to satisfy the CFL condition (ranging from ~2 to ~9 s across simulations). However, for each simulation during the quasi-equilibrium period, the variation of the time step is small. Therefore, there should not be significant sampling error due to uneven sampling throughout the inertial oscillation period.

Under strong wave or destabilizing surface buoyancy forcing, the deepening of the boundary layer is significant during an inertial oscillation period. Direct time averaging will smooth out the sharp stratification at the base of the OSBL and lead to biases in the mean profiles of the turbulence statistics. This effect is significant for $\overline{w'b'}_e$, which occurs right above the boundary layer base. To address this problem, the time series of the horizontal averaged turbulence statistics profiles are stretched or squeezed vertically to match the surface and the boundary layer base ($z = -h_b$) before the time average is taken. An example of $\overline{w'b'}_e$ is given in appendix A.

The time series of $\overline{w'b'}_e$ is relatively noisy (Fig. A1c), presumably due to the intermittent downwelling jet or plumes associated with Langmuir turbulence or convective turbulence. For a few cases, some correlations with the phase of an inertial oscillation is noticeable. To describe uncertainties due to the intermittency of turbulence and the inertial oscillations, the 25th, 50th, and 75th percentiles of $\overline{w'b'}_e$ during an inertial oscillation period are saved and marked as error bars on the corresponding figures. As it is the average over an inertial oscillation period that is of interest in this study, more detailed descriptions of the inertial oscillation-induced variations of $\overline{w'b'}_e$ will be left to be the focus of a future study.

### b. Simulations

In all the simulations presented here, the Stokes drift is assumed to be aligned with the wind. Langmuir turbulence under misaligned wind and waves are discussed in Van Roekel et al. (2012) and McWilliams et al. (2014). The impact of misalignment on $\overline{w'b'}_e$ is unclear. The

Stokes drift profile is computed from the wave frequency spectrum $\Phi(\omega)$ by (Kenyon 1969),

$$u^S(z) = \frac{2}{g}\int_0^\infty \omega^3\Phi(\omega)\exp(2\omega^2 z/g)d\omega. \qquad (1)$$

The empirical spectrum from Donelan et al. (1985, hereinafter DHH) is used to estimate the Stokes drift profile for wind waves under various wind and wave conditions (without directional spreading; Webb and Fox-Kemper 2015),

$$\Phi(\omega) = \alpha g^2\omega^{-4}\omega_p^{-1}\exp[-(\omega_p/\omega)^4]\gamma^{\exp[-(\omega-\omega_p)^2/2\sigma^2\omega_p^2]}, \quad (2)$$

with $\omega_p = g/C_p$ the peak wave frequency (assuming deep water waves); $C_p$ the peak phase speed; and parameters, $\alpha$, $\gamma$, and $\sigma$ as functions of the wave age $C_p/U_{10}$ (where $U_{10}$ is the 10-m wind speed):

$$\alpha = 0.006(C_p/U_{10})^{-0.55},$$

$$\gamma = \begin{cases} 1.7, & 1 < C_p/U_{10} \le 1.2, \\ 1.7 - 6.0\log(C_p/U_{10}), & 0.2 < C_p/U_{10} \le 1, \end{cases} \qquad (3)$$

$$\sigma = 0.08[1 + 4(C_p/U_{10})^3].$$

Note that the surface Stokes drift $u_0^S \equiv u^S(0)$ is not well defined from the DHH spectrum because of the $\omega^{-4}$ tail at high frequencies (for further discussion, see, e.g., Webb and Fox-Kemper 2011; Lenain and Melville 2017). When integrating (1) numerically, a finite cutoff frequency could prevent the resulting $u_0^S$ from approaching infinity. However, such an approach results in an extremely sharp shear of Stokes drift at the surface that is not resolved by the finite vertical grid used in the LES and would lower the fidelity of the simulation (Pearson 2014). In addition, $u_0^S$ is not even used in the LES model, since the Stokes drift is evaluated at the center of each grid cell. Therefore, in the present study $u_0^S$ is defined as the value at the center of the first vertical grid cell ($z = -0.32$ m). This value represents the Stokes drift shear actually being resolved by the finite vertical grid. The same definition also applies to the Stokes drift of a monochromatic wave introduced below. Since only the resolved Stokes drift is accounted for, great care should be taken when comparing the results here with observations and other studies using similar definitions (e.g., Van Roekel et al. 2012), which may have different representations of the full Stokes drift. The surface-layer-averaged Stokes drift $u_{SL}^S$, as will be introduced in (5), is less sensitive to the vertical resolution, especially when the Stokes drift is averaged over the grid layer, rather than interpolated to the grid (Harcourt and D'Asaro 2008).

Simulations forced by Stokes drift calculated from the DHH spectrum with various wave age ($C_p/U_{10}$ = [0.6, 0.8, 1.0, 1.2]) under moderate wind forcing ($U_{10}$ = [5, 8, 10] m s$^{-1}$) are denoted as S-L1 hereinafter. The surface buoyancy flux is set to a value corresponding to a surface cooling of $Q_0 = -5$ W m$^{-2}$.

While the Stokes drift magnitudes associated with wind waves usually decay faster than exponentially (Webb and Fox-Kemper 2011; Breivik et al. 2014, 2016), Stokes drift induced by the remotely generated swell tends to be more narrow banded and thus penetrates deeper relative to surface drift. To assess the possible sensitivities of the turbulence statistics to the shape of the Stokes drift profile, a few simulations are performed with Stokes drift profiles associated with a monochromatic wave $k = \omega^2/g$ and wave amplitude $A$,

$$u^S(z) = \omega k A^2\exp(2kz). \qquad (4)$$

This Stokes drift profile was used in many previous LES studies (e.g., McWilliams et al. 1997; Grant and Belcher 2009). Simulations forced by Stokes drift calculated from (4) with wavenumber of $k = 0.10$ m$^{-1}$ and various wave amplitude ($A$ = [0.40, 0.53, 0.80] m) are denoted as S-L2 hereinafter.

To cover the transition from Langmuir turbulence to convective turbulence, simulations with various surface cooling ($Q_0$ = [−10, −25, −50, −100, −200, −300, −500] W m$^{-2}$) under moderate wind forcing ($U_{10}$ = [5, 8, 10] m s$^{-1}$) were performed.[2] For each combination of wind and surface cooling, a young and a fully developed wind-wave case, corresponding to wave ages of $C_p/U_{10}$ = [0.8, 1.2], explore the effects of Langmuir turbulence under strongly convective conditions. Hereinafter, this set of simulations is denoted as S-B.

Finally, for each combination of wind and surface buoyancy forcing described above, there is a corresponding wave-free simulation to cover the transition from (wave-free) shear turbulence to (wave-free) convective turbulence, that is, identical to the previous runs except with zero Stokes drift at all depths and no Langmuir turbulence. This set of simulations is denoted as S-NL hereafter. For quick reference, all the simulations are summarized in Table 1.

### c. Parameter space

In addition to $u_0^S$, another choice of the velocity scale for the wave forcing is the surface-layer-averaged Stokes drift, introduced by Harcourt and D'Asaro (2008):

---

[2] For surface wind forcing of $U_{10}$ = [8, 10] m s$^{-1}$, fewer simulations were performed, namely, with surface cooling of $Q_0$ = [−25, −50, −100] W m$^{-2}$.

TABLE 1. Summary of simulations. Each column represents, respectively, the case name, the 10-m wind forcing, the surface heat flux, the wave age for DHH wind-wave forcing (1), the wavenumber, and the wave amplitude for monochromatic wave forcing (4). For cases S-B and S-NL with surface wind forcing of $U_{10} = [8, 10]\ \mathrm{m\,s^{-1}}$, fewer simulations were performed, as indicated by italics.

| Case | $U_{10}$ (m s$^{-1}$) | $-Q_0$ (W m$^{-2}$) | $C_p/U_{10}$ | $k$ (m$^{-1}$) | $A$ (m) |
|---|---|---|---|---|---|
| S-L1 | [5, 8, 10] | 5 | [0.6, 0.8, 1.0, 1.2] | — | — |
| S-L2 | [5, 8, 10] | 5 | — | 0.1 | [0.4, 0.53, 0.8] |
| S-B | [5, *8*, *10*] | [10, *25*, *50*, *100*, 200, 300, 500] | [0.8, 1.2] | — | — |
| S-NL | [5, *8*, *10*] | [5, 10, *25*, *50*, *100*, 200, 300, 500] | — | — | — |

$$u^S_{\mathrm{SL}} \equiv \langle u^S \rangle_{H_{\mathrm{SL}}} = \frac{1}{H_{\mathrm{SL}}}\int_{-H_{\mathrm{SL}}}^{0} u^S(z)\,dz\,, \qquad (5)$$

where $H_{\mathrm{SL}} = h_b/5$ is the depth of the surface layer and is taken as the upper 20% of the boundary layer here, and $\langle\cdot\rangle_h$ denotes the depth average over a layer from $z = -h$ to $z = 0$. It has been shown that scalings using $u^S_{\mathrm{SL}}$ can better collapse the results with various wind and wave forcing (Harcourt and D'Asaro 2008; Van Roekel et al. 2012). As will be shown later, the improved consistency of this metric is also supported by simulations in this study.

Similar to the turbulent Langmuir number defined by McWilliams et al. (1997),

$$\mathrm{La_t} = (u^*/u^S_0)^{1/2}\,, \qquad (6)$$

the surface layer turbulent Langmuir number (Harcourt and D'Asaro 2008) can be defined from (5),

$$\mathrm{La_{SL}} = [u^*/(u^S_{\mathrm{SL}} - u^S_{\mathrm{ref}})]^{1/2}\,, \qquad (7)$$

where $u^S_{\mathrm{ref}}$ is the Stokes drift at a reference level (here at the base of the boundary layer and $u^S_{\mathrm{ref}} \approx 0$ given the Stokes drift profiles used in this study). Profile $u^S_{\mathrm{ref}}$ is subtracted from $u^S_{\mathrm{SL}}$ to represent the mean vertical shear of Stokes drift in the boundary layer. The drag coefficient from Large and Pond (1981) is used to relate $u^*$ to $U_{10}$. Both definitions of Langmuir number measure the relative importance of shear turbulence and Langmuir turbulence.

A measure of the relative penetration depth of Stokes drift is quantified by the ratio

$$D^S = \delta^S/h_b\,, \qquad (8)$$

where $\delta^S$ is the Stokes depth, defined by

$$\delta^S = 1/2k \qquad (9)$$

for monochromatic waves and approximated by

$$\delta^S = \frac{1}{u^S_0}\int_{-\infty}^{0} u^S dz \qquad (10)$$

for wind waves.

Finally, a measure of the relative importance of convective turbulence and shear turbulence is given by

$$-h_b/(\kappa L) = B_0 h_b/u^{*3} = w^{*3}/u^{*3}\,. \qquad (11)$$

Alternatively, one can use the measure of relative importance of convective turbulence and Langmuir turbulence (Belcher et al. 2012),[3]

$$h_b/L_L = B_0 h_b/(u^{*2}u^S) = -\mathrm{La}_t^2 h_b/(\kappa L)\,. \qquad (12)$$

The parameter space covered by each subset of the simulations in this study is summarized in Table 2. As an example, Fig. 2a displays the coverage in the $\mathrm{La}_t$–$h_b/L_L$ regime diagram introduced by Belcher et al. (2012). The transition from Langmuir turbulence to convection is reasonably well covered by the simulations in this study. The parameter space covered here appears to represent the typical Southern Ocean conditions in the regime diagram as identified by Belcher et al. (2012), and the typical conditions in a global climate model (light gray contours). The joint distribution of $\mathrm{La}_t$ and $h_b/L_L$ is estimated from the daily averaged output in a typical simulated year of a global fully coupled Community Earth System Model (CESM) simulation (PI-WW3 in Li et al. 2017). Note that only situations with destabilizing surface buoyancy flux are shown here, which represent about 40% of the total in a simulated year. The diurnal cycle is highly parameterized in CESM (Large and Caron 2015) and not represented in this estimate. In addition, a single point in the regime diagram could possibly represent multiple real conditions in dimensional space, with various other parameters not

---

[3] Note that in Belcher et al. (2012) the mixed layer depth $h_m$, instead of the boundary layer depth $h_b$, is used as the length scale of the OSBL. The differences are negligible for the purpose here. However, using $h_b$ as the length scale does result in slightly better scalings in most cases in this study. Therefore, $h_b$ is used throughout this paper unless otherwise noted.

TABLE 2. Summary of the dimensionless parameters. The minimum and maximum values of each parameter are listed for each subset of the simulations. See section 2c for the definitions and physical interpretations of the dimensionless parameters.

| Case | $\mathrm{La}_t$ | $\mathrm{La}_{\mathrm{SL}}$ | $D^S$ (%) | $H_b/L_L$ | $-h_b/(\kappa L)$ |
|---|---|---|---|---|---|
| S-L1 | 0.26–0.80 | 0.50–2.83 | 1.6–4.7 | 0.0048–0.33 | 0.072–0.53 |
| S-L2 | 0.31–0.87 | 0.45–1.34 | 9.2–10.4 | 0.014–0.20 | 0.073–0.53 |
| S-B | 0.26–0.55 | 0.50–2.17 | 1.3–5.9 | 0.025–24.5 | 0.37–82.7 |
| S-NL | — | — | — | — | 0.070–79.2 |

included in the regime diagram. Figure 2b compares the dissipation rate at the center of the boundary layer from our simulations to the prediction given by Belcher et al. (2012). Reasonable consistencies are found, though less so when Langmuir turbulence dominates.

## 3. Turbulence statistics

### a. *Effect of Stokes depth*

Figure 3 shows the vertical profiles of the turbulence statistics for simulations under various wave forcing (S-L1 and S-L2). For clarity only the weak wind cases ($U_{10} = 5\,\mathrm{m\,s^{-1}}$) are shown here. Simulations with higher wind speed show qualitatively similar patterns, though quantitative differences exist. In Fig. 3a, $u_0^S$ and $u_{\mathrm{SL}}^S$ are marked by the upper and lower groups of vertical lines. The presence of Stokes drift, which introduces a new length scale $\delta^S$, modifies the shape of the turbulence statistics profiles in addition to their magnitude. Therefore, no attempt is made to collapse all the profiles here.

Visual examination of Fig. 3c shows that similar $\overline{w'b'}_e$ may result from different $u_0^S$ (e.g., comparing the solid curve in blue versus the dash–dotted curve in cyan); on the other hand, similar $u_0^S$ may lead to very different $\overline{w'b'}_e$ (e.g., comparing the dashed curve in blue and the dash–dotted curve in cyan). Entrainment buoyancy flux ($\overline{w'b'}_e$) correlates better with $u_{\mathrm{SL}}^S$ than $u_0^S$, though not perfectly, as is also observed for correlations with Lagrangian shear production, TKE transport, and dissipation.

### b. *Langmuir turbulence versus convective turbulence*

Figure 4 displays profiles of $\overline{w'^2}$, $\overline{w'b'}$, and dissipation for simulations under various surface cooling (distinguished

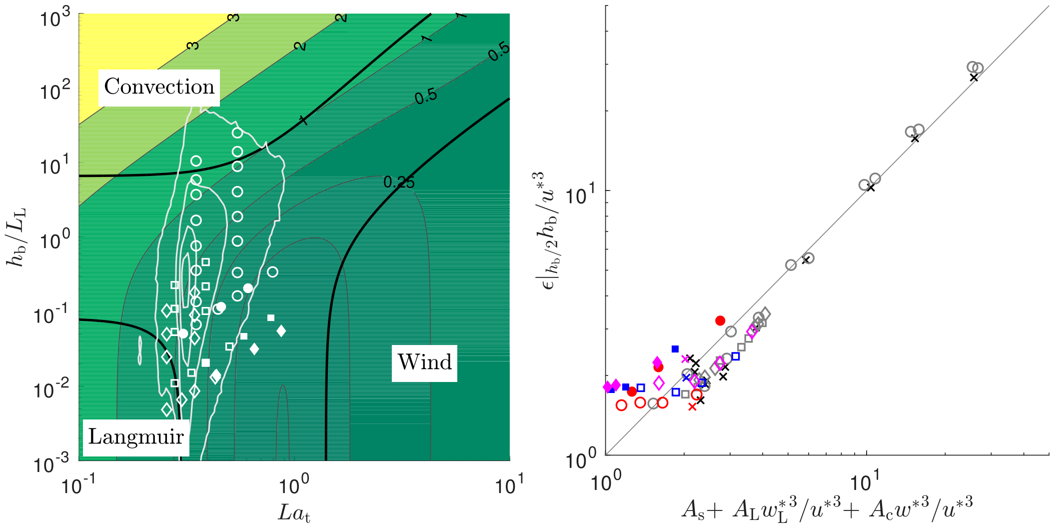

(a) (b)

FIG. 2. (a) Reproducing the regime diagram described in Belcher et al. (2012). Overlaid white symbols mark all the wave forced simulations in this study. The light gray contours show the highest 30%, 60%, 90%, and 99% centered distribution of $\mathrm{La}_t$ and $h_b/L_L$, estimated from the daily averaged output in one simulated year of a global fully coupled CESM simulation (PI-WW3 in Li et al. 2017). Note that only situations with destabilizing surface buoyancy flux are shown here, which represent about 40% of the total in a simulated year. (b) The normalized dissipation at the center of the boundary layer $\varepsilon h_b/u^{*3}$ vs the prediction in Belcher et al. [2012, their Eq. (5)], with $A_s = 2\{1 - \exp[-(1/2)\mathrm{La}_t]\}$, $A_L = 0.22$, and $A_c = 0.3$. The shape and color (if applicable) of the symbols are coded as follows. Crosses mark results from the subset S-NL (no Langmuir), whereas other symbols represent results from the other three subsets, with circles, squares, and diamonds corresponding to 10-m wind of 5, 8, and $10\,\mathrm{m\,s^{-1}}$, respectively. Results from the subsets S-L1 (wind waves) and S-L2 (monochromatic), as well as the corresponding no-Langmuir simulations in S-NL, are highlighted in color, and distinguished by empty (S-L1) and filled (S-L2) symbols. Results from subset S-B (waves and convection) are colored in gray.

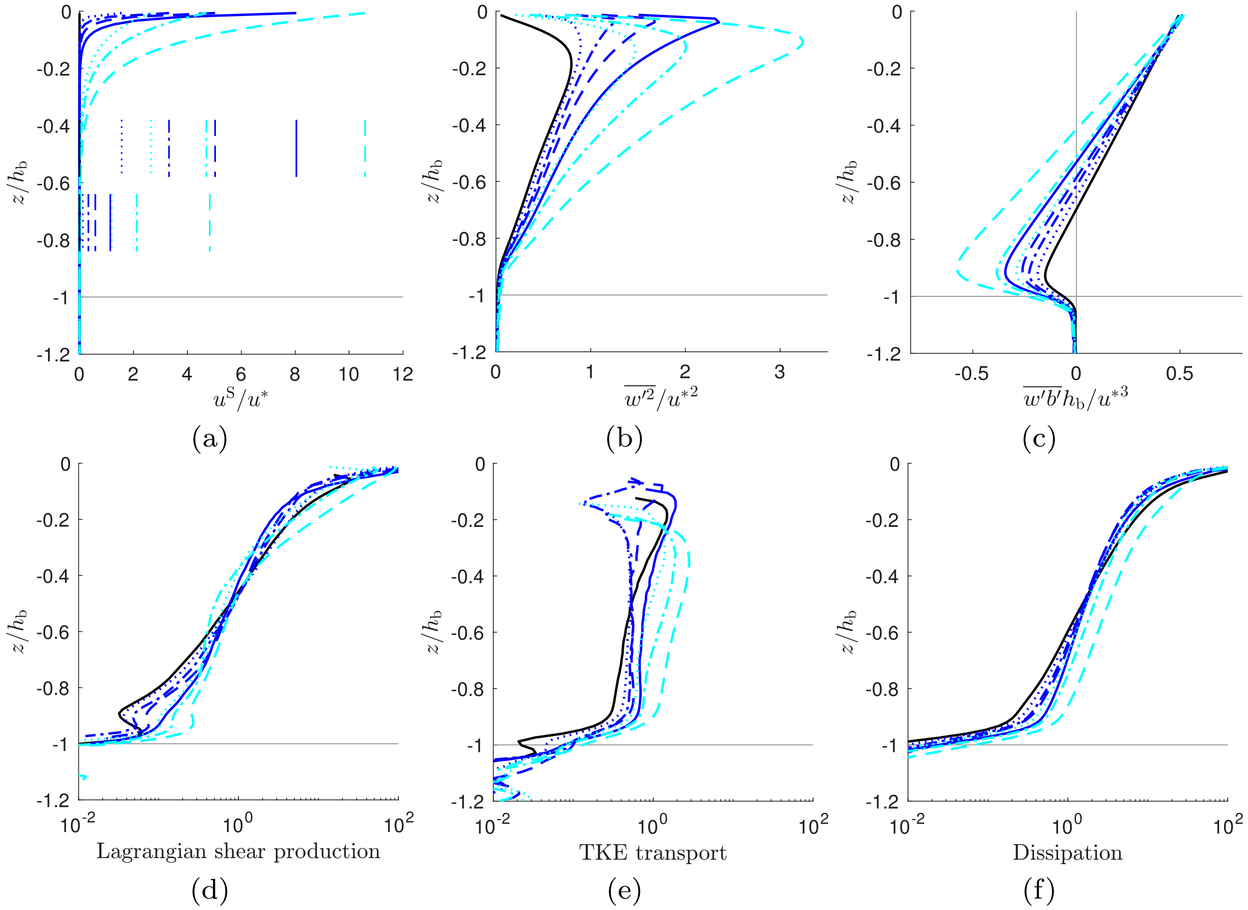

FIG. 3. Vertical profiles of the turbulence statistics under various wave forcing for S-L1 (blue) and S-L2 (cyan). For clarity only the results with weak wind forcing ($U_{10} = 5\ \mathrm{m\,s^{-1}}$) are shown. Four cases in S-L1 with different wave ages (0.6–1.2) are represented by dotted, dashed–dotted, dashed, and solid curves, respectively. Three cases in S-L2 with different wave amplitudes (0.4–0.8 m) are represented by dotted, dashed–dotted, and dashed curves, respectively. (a) $u^S/u^*$; the upper and lower group of vertical lines highlight $u_0^S$ and $u_{\mathrm{SL}}^S$, respectively, for each case. (b) $\overline{w'^2}/u^{*2}$. (c) $\overline{w'b'}h_b/u^{*3}$. (d) Normalized Lagrangian shear production (Eulerian shear production + Stokes production). (e) Normalized TKE transport. (f) Normalized dissipation. Panels (d)–(f) are normalized by $u^{*3}/h_b$.

by colors) and wave forcing (distinguished by line styles). The Langmuir turbulence induced enhancement on $\overline{w'^2}$ and $\overline{w'b'}$, respectively, appear to be similar when normalized by functions of $u^*$ (Figs. 4a,c), but significantly different when normalized by functions of $w^*$ (Figs. 4b,d). This suggests that Langmuir turbulence has a much weaker effect on convective turbulence than on shear turbulence. Therefore, to leading order—and proposed parameterization accuracy—the correction to account for the effects of Langmuir turbulence on both $\overline{w'^2}$ and $\overline{w'b'}$ can be written out as a multiplier on the shear turbulence contribution but not on the convective turbulence contribution.

The mixed layer–averaged vertical velocity variance $\langle \overline{w'^2} \rangle_{h_m}$ is a metric used to describe the intensity of the ocean surface vertical mixing (e.g., D'Asaro 2001; Tseng and D'Asaro 2004; Harcourt and D'Asaro 2008; Van Roekel et al. 2012; D'Asaro 2014; D'Asaro et al. 2014). In Fig. 5, $\langle \overline{w'^2} \rangle_{h_m}/u^{*2}$ is plotted against $w^{*2}/u^{*2}$, $\mathrm{La}_t^{-2} = u_0^S/u^*$, and $\mathrm{La}_{\mathrm{SL}}^{-2} = u_{\mathrm{SL}}^S/u^*$ to show the effects of convective turbulence and Langmuir turbulence on the vertical mixing. Consistent with previous studies on free convection and wall-bounded shear turbulence, $\langle \overline{w'^2} \rangle_{h_m}$ is approximately proportional to $w^{*2}$ in the convective turbulence regime ($w^{*2}/u^{*2}$) and proportional to $u^{*2}$ in the shear turbulence regime ($w^{*2}/u^{*2}$). The presence of Langmuir turbulence enhances the vertical mixing in both regimes, but behaves very differently (Fig. 5a).

Under weak surface cooling (colored symbols in Figs. 5b,c), $\langle \overline{w'^2} \rangle_{h_m}/u^{*2}$ scales with $\mathrm{La}_t^{-2}$ and $\mathrm{La}_{\mathrm{SL}}^{-2}$ reasonably well. The results shown here are generally consistent with the scaling laws proposed in previous studies (e.g., Harcourt and D'Asaro 2008; Van Roekel

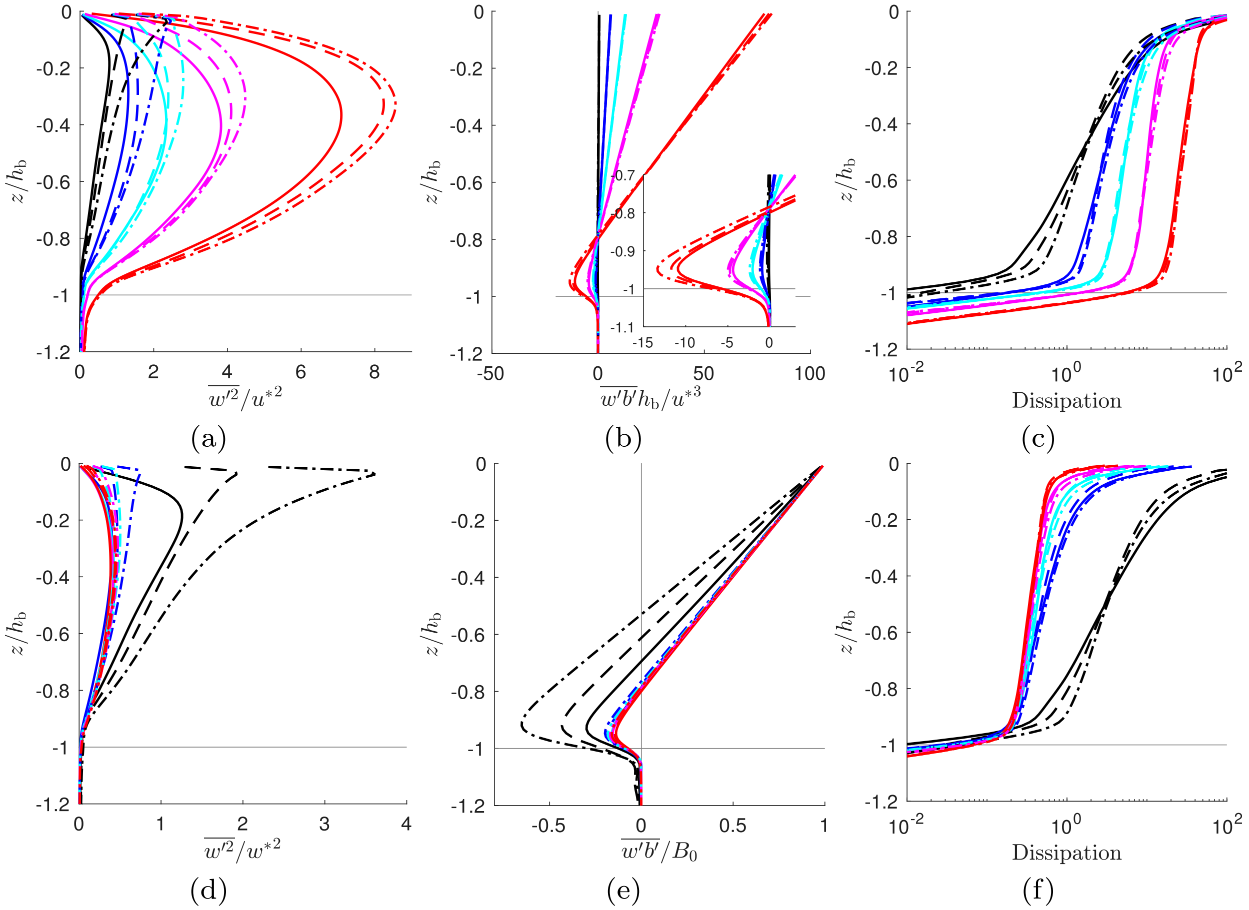

FIG. 4. Vertical profiles of the turbulence statistics under various surface cooling: (a) $\overline{w'^2}/u^{*2}$, (b) $\overline{w'b'}h_b/u^{*3}$, (c) dissipation normalized by $u^{*3}/h_b$, (d) $\overline{w'^2}/w^{*2}$, (e) $\overline{w'b'}/B_0$, and (f) dissipation normalized by $B_0$. All the cases shown here are forced by 5 m s$^{-1}$ surface wind with various surface coolings of $-5$, $-50$, $-100$, $-200$, and $-500$ W m$^{-2}$, represented by black, blue, cyan, magenta, and red, respectively. In each colored group, the solid, dashed, and dashed–dotted lines illustrate increasing wave forcing, corresponding to wave-free, young ($C_p/U_{10} = 0.8$), and developed wind waves ($C_p/U_{10} = 1.2$) from the DHH spectrum, respectively.

et al. 2012). Smaller root-mean-square (RMS) differences from the scaling laws are found when $\langle\overline{w'^2}\rangle_{h_m}/u^{*2}$ is scaled with $\mathrm{La}_{\mathrm{SL}}^{-2}$ ($\sim$0.10, versus $\sim$0.15 when scaled with $\mathrm{La}_t^{-2}$), which partially accounts for the effects of Stokes depth. Also noticeable are the clearly distinguished slopes projected by the filled and empty colored symbols, respectively, in Fig. 5b. It is interesting to note that the dotted curves in Figs. 5b and 5c, which connect results with the same surface buoyancy forcing, all have similar slopes. This suggests that most of the Langmuir-turbulence-induced variations of $\langle\overline{w'^2}\rangle_{h_m}/u^{*2}$ are explained by a dependence on the Langmuir number, and this effect is additive rather than multiplicative to the convective turbulence-induced variations.

Indeed, Langmuir turbulence and convective turbulence share some similarities in enhancing the vertical mixing. Namely, the intermittent downwelling jets associated with the Langmuir circulation (Polton and Belcher 2007) driven by the Stokes shear force (Suzuki and Fox-Kemper 2016) are reminiscent of the downwelling plumes driven by the buoyancy force in convection. Though unlike the buoyancy force, which acts on a less buoyant water parcel and accelerates the downwelling motion all the way down to the base of the mixed layer, the Stokes shear force is confined within the Stokes shear layer, acting as an initial pump. Nevertheless, this enhancement of vertical mixing is associated with modifications of the turbulence anisotropy within the OBSL. Displayed in Fig. 6 are the ratio of the total vertical turbulent kinetic energy (VKE) to the total TKE, plotted against $w^{*2}/u^{*2}$, $\mathrm{La}_t^{-2}$, and $\mathrm{La}_{\mathrm{SL}}^{-2}$. As shown by the crosses, this ratio is about 0.15 for pure shear turbulence without Langmuir turbulence and approaches 1/3 for the convective turbulence. The presence of the Langmuir turbulence enhances the VKE significantly, pushing the ratio of VKE/TKE toward

1/3 as wave forcing is strengthened. Note that for isotropic turbulence the ratio VKE/TKE is 1/3, although a ratio of 1/3 is not sufficient to guarantee isotropy. Indeed, anisotropy is strong in Langmuir turbulence, especially in the horizontal direction. Here the ratio VKE/TKE is used as a bulk measure of the turbulence anisotropy in the mixed layer, which is dominated by coherent structures at the energy containing scale. Near the grid scale, isotropy is generally recovered, except near the surface where distortions by Eulerian shear and Stokes drift are strong, and in the entrainment layer where buoyancy effects are significant.[4] Detailed discussion of the turbulent structures is left to future study.

### c. *Implications for the Langmuir mixing parameterization in KPP*

Wave-induced mixing can be parameterized in KPP by applying a Langmuir-number-related enhancement factor on the turbulent velocity scale $w_x$ (McWilliams and Sullivan 2000; Smyth et al. 2002; Li et al. 2016). Note that the scaling laws used in those parameterizations were found to match LES with rather weak surface buoyancy fluxes, but strong wind and wave forcing. However, pure shear turbulence, with a velocity scale of $u^*$, and convective turbulence, with a velocity scale of $w^*$, jointly contribute to the turbulent velocity scale in KPP, for example, $w_x \sim (c_1 u^{*3} + c_2 w^{*3})^{1/3}$ with $c_1$ and $c_2$ some constants. Simply applying the Langmuir enhancement factor to the turbulent velocity scale implies similar Langmuir enhancement on turbulence generated by both shear and convective mechanisms. In contrast, the preceding results indicate that enhanced mixing due to waves appears to be additive in the case of convective-turbulence-induced mixing, rather than multiplicative as in shear-turbulence-induced mixing. Therefore, the simplest approach capturing this effect is to apply the Langmuir enhancement factor only to the shear turbulence component of the turbulent velocity scale and not on the convective turbulence component (or the total).

The consideration of a reduced enhancement factor under strongly unstable conditions (convective turbulence regime) marks a major modification by Smyth et al. (2002) to the enhancement factor formula proposed by McWilliams and Sullivan (2000). This effect is also implicitly accounted for in the formula adopted by Li et al. (2016) by using $\mathrm{La}_{\mathrm{SL}}$ instead of $\mathrm{La}_t$. Under strong convective conditions, rapid deepening of the boundary layer depth quickly decreases $u^S_{\mathrm{SL}}$ under fixed waves, so the resulting enhancement factor approaches one. Therefore, significantly different results from Li et al. (2016) are not expected under the strongest convective forcing by applying the enhancement factor only to the shear turbulence component of the turbulent velocity scale. Nevertheless, great care should be taken when interpreting the physical meaning of the enhancement factor.

### d. *A velocity scale for the entrainment buoyancy flux?*

The RMS vertical velocity $(\langle\overline{w'^2}\rangle_{h_m})^{1/2}$ provides a useful velocity scale describing the intensity of the turbulence that drives the vertical mixing *within the mixed layer*. Some parameterization schemes have been focused on the effect of Langmuir turbulence on the scaling of $(\langle\overline{w'^2}\rangle_{h_m})^{1/2}$ (e.g., Harcourt and D'Asaro 2008; Van Roekel et al. 2012; D'Asaro et al. 2014). An interesting question to ask is whether this velocity scale predicts the variations of $\overline{w'b'}_e$, that is, *within the entrainment layer*? If so, then there is no need to find a new scaling for $\overline{w'b'}_e$, but just an appropriate method for lower boundary condition matching. To answer this question, the magnitude of $\overline{w'b'}_e$ is normalized by $(\langle\overline{w'^2}\rangle_{h_m})^{3/2}/h_b$ and plotted against $w^{*2}/u^{*2}$ and $\mathrm{La}_{\mathrm{SL}}^{-2}$ in Fig. 7. A positive constant would be expected if $(\langle\overline{w'^2}\rangle_{h_m})^{1/2}$ is a good predictor of the velocity scale for entrainment. Indeed, the normalized magnitude of $\overline{w'b'}_e$ is $O(1)$, that is, $(\langle\overline{w'^2}\rangle_{h_m})^{3/2}/h_b$ explains much variability in $\overline{w'b'}_e$. However, the factor of 3 or so residual dependence of entrainment on both $w^{*2}/u^{*2}$ and $\mathrm{La}_{\mathrm{SL}}^{-2}$ suggests that an improved scaling law for $\overline{w'b'}_e$ itself is possible.

## 4. Scaling the entrainment buoyancy flux

In equilibrium state, with waves oriented down the $x$ axis, the temporal and horizontal mean TKE budget is given by (e.g., McWilliams et al. 1997; Grant and Belcher 2009)

$$0 = \underbrace{-\overline{u'w'}\frac{\partial \overline{u}}{\partial z} - \overline{v'w'}\frac{\partial \overline{v}}{\partial z}}_{\text{shear prod.}} - \underbrace{\overline{u'w'}\frac{\partial u^S}{\partial z}}_{\text{Stokes}} + \underbrace{\overline{w'b'}}_{\text{buoy.}} - \underbrace{\frac{\partial}{\partial z}\left(\frac{\overline{w'p'}}{\rho_0}\right)}_{\text{press. trans.}} + \underbrace{\frac{\partial \overline{w'e}}{\partial z}}_{\text{TKE trans.}} - \underbrace{\varepsilon}_{\text{diss.}}. \tag{13}$$

The terms on the right-hand side of (13) represent the shear production (along- and across-wind direction components), the Stokes production, the buoyancy production,

---

[4] Near the surface, distortions by the wind-driven shear and Stokes drift enhance the along-wind and vertical velocity fluctuations, respectively, on a broad range of scales (Teixeira and Belcher 2010). In the entrainment layer, the mean Ozmidov scale $L_O = \sqrt{\varepsilon/N^3}$ (e.g., Smyth and Moum 2000) ranges from 0.059 to 0.65 m and is smaller than the vertical resolution (0.64 m) in our simulations, indicating that buoyancy effects are important there even near grid scale.

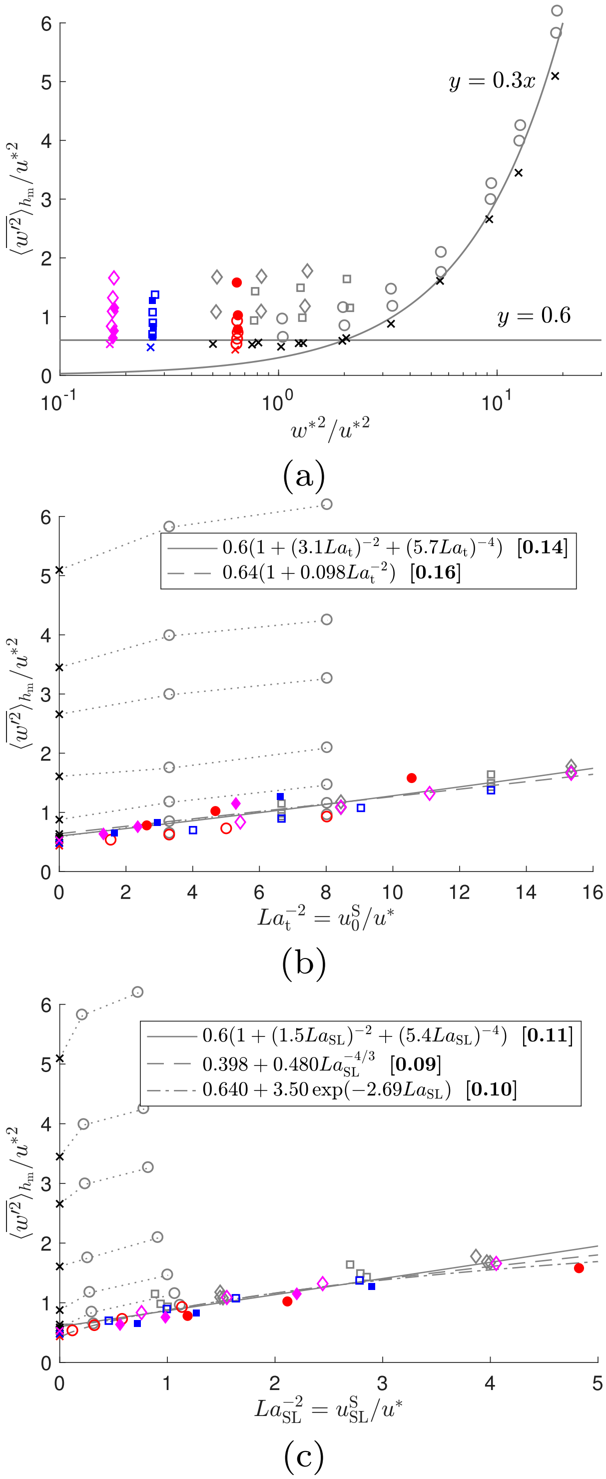

FIG. 5. The impact of surface cooling and wave forcing on the mean vertical velocity variance: $\langle \overline{w'^2} \rangle_{h_m}/u^{*2}$ is plotted against (a) $w^{*2}/u^{*2}$, (b) $\mathrm{La}_t^{-2} = u_0^S/u^*$, and (c) $\mathrm{La}_{SL}^{-2} = u_{SL}^S/u^*$. The solid curves in (a) illustrate the canonical values in the shear turbulence regime $\langle \overline{w'^2} \rangle_{h_m} \approx 0.6u^{*2}$ and the convective turbulence regime $\langle \overline{w'^2} \rangle_{h_m} \approx 0.3w^{*2}$. Solid, dashed, and dashed–dotted curves in (b) and (c) illustrate the scaling laws proposed in Harcourt and D'Asaro (2008) and Van Roekel et al. (2012), with the RMS differences of all the nonconvection cases from the scaling laws listed in brackets. Dotted curves connect simulations with the same surface buoyancy forcing. Symbols are as in Fig. 2.

the pressure transport, the TKE transport (where $e$ represents the TKE), and the dissipation, respectively.

For simplicity, the typical buoyancy flux profile depicted in Fig. 1a is approximated by

$$\overline{w'b'}(z) = \begin{cases} B_0\left(1 + \dfrac{z}{h_m}\right) - \overline{w'b'}_e \dfrac{z}{h_m}, & -h_m < z \le 0, \\ \overline{w'b'}_e \dfrac{h_b + z}{h_b - h_m}, & -h_b < z \le -h_m, \\ 0, & z \le -h_b. \end{cases} \tag{14}$$

Integrating (14) over the boundary layer gives the total conversion of TKE to potential energy,

$$\int_{-h_b}^{0} \overline{w'b'} dz = \frac{1}{2} B_0 h_m + \frac{1}{2} \overline{w'b'}_e h_b. \tag{15}$$

For simplicity the transport terms at the surface and the base of the boundary layer are assumed to be zero. However, processes that are not considered in this study, such as breaking surface waves (e.g., Sullivan et al. 2007), and high-frequency internal waves below the boundary layer generated by Langmuir motions (Polton et al. 2008) may lead to nonzero fluxes at the upper and lower boundaries and contribute to the integrated TKE budget, though in general the energy flux to internal waves is small compared with the loss to dissipation and mixing within the OSBL (e.g., Wunsch and Ferrari 2004). With that in mind, the integrated TKE budget gives,

$$-\overline{w'b'}_e = \frac{2}{h_b} \int_{-h_b}^{0} \left( -\overline{u'w'} \frac{\partial \overline{u}}{\partial z} - \overline{v'w'} \frac{\partial \overline{v}}{\partial z} \right) dz + \frac{2}{h_b} \int_{-h_b}^{0} \left( -\overline{u'w'} \frac{\partial u^S}{\partial z} \right) dz + B_0 \frac{h_m}{h_b} - \frac{2}{h_b} \int_{-h_b}^{0} \varepsilon dz. \tag{16}$$

Considering the scaling of each term on the right-hand side individually, the first term scales with $u^{*3}/h_b$ and the second term scales with $u^{*2}u_0^S/h_b$ (e.g., Grant and Belcher 2009). These scalings result from the arguments that $\langle \overline{u'w'} \rangle_{h_b} \sim \langle \overline{v'w'} \rangle_{h_b} \sim u^{*2}$, $\langle \partial \overline{u}/\partial z \rangle_{h_b} \sim \langle \partial \overline{v}/\partial z \rangle_{h_b} \sim u^*/h_b$, and $\langle \partial u^S/\partial z \rangle_{h_b} \sim u_0^S/h_b$. However, such arguments ignore the effects of the Stokes drift on the Eulerian velocity,

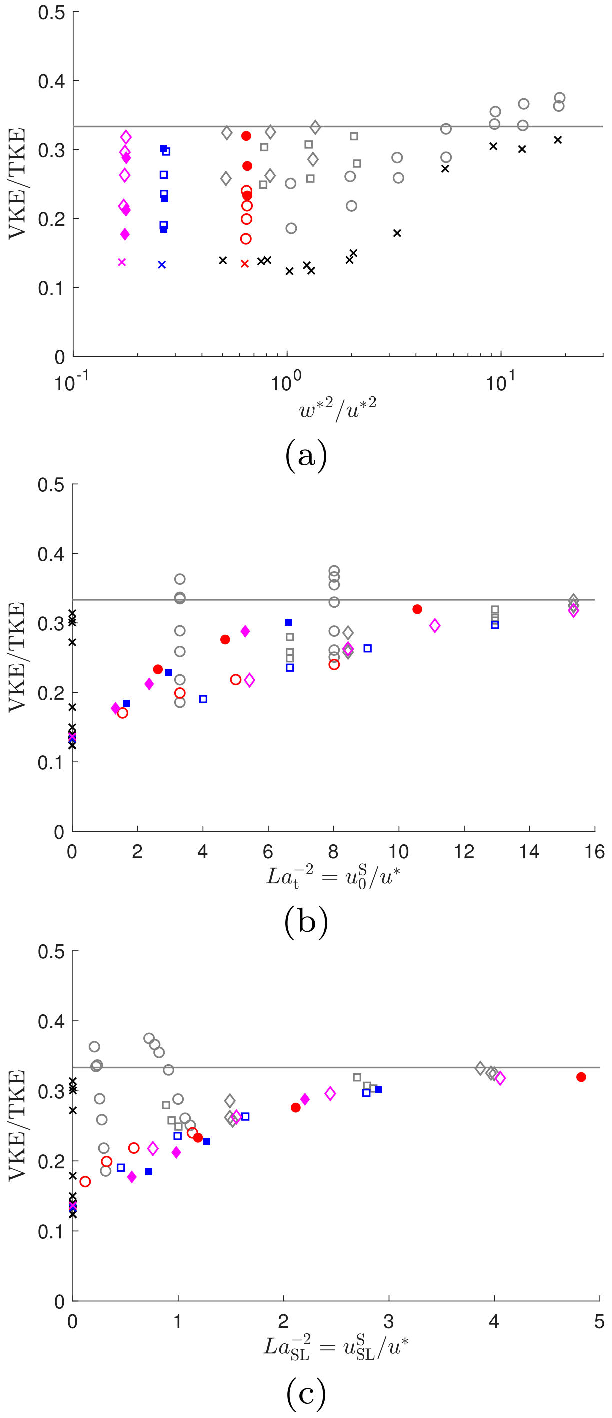

(a)

(b)

(c)

FIG. 6. The impact of surface cooling and wave forcing on the turbulence anisotropy. The ratio VKE/TKE is plotted against (a) $w^{*2}/u^{*2}$, (b) $\mathrm{La}_t^{-2} = u_0^S/u^*$, and (c) $\mathrm{La}_{\mathrm{SL}}^{-2} = u_{\mathrm{SL}}^S/u^*$. The gray line marks the value of 1/3. Symbols are as in Fig. 2.

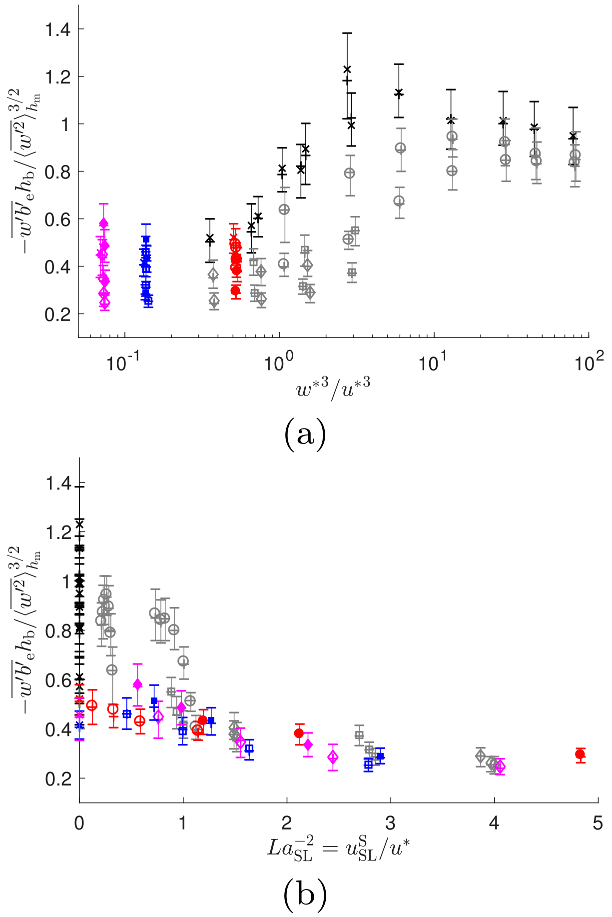

(a)

(b)

FIG. 7. The magnitude of $\overline{w'b'}_e$ is normalized by $\left(\langle\overline{w'^2}\rangle_{h_m}\right)^{3/2}/h_b$ and plotted against (a) $w^{*2}/u^{*2}$ and (b) $\mathrm{La}_{\mathrm{SL}}^{-2} = u_{\mathrm{SL}}^S/u^*$. Error bars show the 25th, 50th, and 75th percentiles within an inertial oscillation period. Symbols are as in Fig. 2.

namely, the "anti-Stokes" effect (McWilliams and Fox-Kemper 2013; Haney et al. 2015). In the presence of Stokes drift, the Eulerian shear is reduced to partially cancel the added production from Stokes shear. The resulting Eulerian shear is generally smaller in the upper part of the OSBL and greater in the lower part than it would be under the same wind forcing without Stokes drift. In addition, the adjustment of the Eulerian velocity should also depend on the decay depth of the Stokes drift. Given the above considerations, it appears to be more appropriate to scale the Lagrangian shear production (Eulerian shear + Stokes production) all together with $u^{*3}\mathscr{F}(\mathrm{La}_x)/h_b$, where $\mathscr{F}(\cdot)$ is a function that returns a dimensionless number and $\mathrm{La}_x$ represents either $\mathrm{La}_t$ or $\mathrm{La}_{\mathrm{SL}}$.

Since the ratio $h_m/h_b$ remains approximately a constant ($\approx$1), especially in the convective limit (Fig. 1), the third term in (16) should scale with $w^{*3}/h_b$. The remaining term to scale in (16) is the total dissipation. It is convenient practice to assume that the integrated dissipation is composed of terms that are individually proportional to each of the production terms (e.g., Niiler and Kraus 1977; Belcher et al. 2012). Directly diagnosing the ratios of the integrated dissipation to the Lagrangian shear production and the surface buoyancy forcing, respectively, in LES generally support this assumption (not shown). Therefore, the dissipation term can be absorbed in the scaling of each of the production terms, and (16) is written as

$$-\overline{w'b'}_e = c_{\mathrm{ST}}\frac{u^{*3}}{h_b}\mathscr{F}(\mathrm{La}_x) + c_{\mathrm{CT}}\frac{w^{*3}}{h_b}. \qquad (17)$$

Here $c_{\mathrm{ST}}$, $c_{\mathrm{CT}}$ and $c_{\mathrm{LT}}$ (below) are dimensionless constants to be determined. Each term represents the contribution from a single source: ST for shear turbulence, CT for convective turbulence, and LT for Langmuir turbulence. Note that although $-\overline{w'b'}_e$ is a component of the layer-integrated buoyancy production term in (13), it essentially represents the conversion of TKE to potential energy and is a sink of TKE. Thus, there is no need to absorb a portion of the dissipation into this term.

Considering the fact that $\mathscr{F}(\mathrm{La}_x) \to 1$ as $\mathrm{La}_x \to +\infty$ in the wave-free limit and $\mathscr{F}(\mathrm{La}_x)$ should increase with decreasing $\mathrm{La}_x$, a simple functional form,

$$\mathscr{F}(\mathrm{La}_x) = 1 + \frac{c_{\mathrm{LT}}}{c_{\mathrm{ST}}}\mathrm{La}_x^{-p}, \qquad (18)$$

is tested with free parameters $c_{\mathrm{LT}}$ and $p$ to fit the data from all the simulations. The proportionality coefficient in (18) is written in a form that, when substituted into (17), gives

$$-\overline{w'b'}_e = c_{\mathrm{ST}}\frac{u^{*3}}{h_b} + c_{\mathrm{LT}}\frac{u^{*3}}{h_b}\mathrm{La}_x^{-p} + c_{\mathrm{CT}}\frac{w^{*3}}{h_b}. \qquad (19)$$

The three terms on the right-hand side of the equation represent the entrainment buoyancy flux due to the shear turbulence, enhancement due to the Langmuir turbulence, and contributions from the convective turbulence. Note that the choice of this form is made simply for mathematical convenience for application within KPP and different frameworks that fit the same LES data (B. G. Reichl et al. 2017, unpublished manuscript). The second term does not uniquely represent the Stokes production term in (16). Instead, it represents all changes due to Stokes drift in the scaling, which affects both the Stokes production and Eulerian shear production through the anti-Stokes effect, even beyond changes to the turbulence covariances.

With any given power $p$, the three coefficients could simply be estimated from the linear least squares regression by writing (19) as

$$-\frac{\overline{w'b'}_e h_b}{u^{*3}} = c_{\mathrm{ST}} + c_{\mathrm{LT}}\mathrm{La}_x^{-p} + c_{\mathrm{CT}}\frac{w^{*3}}{u^{*3}}. \qquad (20)$$

Estimates of $c_{\mathrm{ST}}$, $c_{\mathrm{LT}}$, and $c_{\mathrm{CT}}$ for various $p$ and both $\mathrm{La}_x = \mathrm{La}_t$ and $\mathrm{La}_x = \mathrm{La}_{\mathrm{SL}}$ are tested to fit separately all and two subsets (S-NL and S-L1 + S-L2) of the data (see more details in appendix B). It is found that $\mathrm{La}_x = \mathrm{La}_{\mathrm{SL}}$ and $p = 2$ give consistent estimates of the three coefficients. Separate curve-fitting results with data from subsets S-NL and S-L1 + S-L2 are shown in Figs. 8a and 8c, respectively. The estimation $c_{\mathrm{CT}} \approx 0.15$ is robust due to a variety of simulations in the convective turbulence regime.[5] As a result of the relatively narrow range of $\mathrm{La}_{\mathrm{SL}}^{-2}$, estimations for the other two coefficients might be less robust: $c_{\mathrm{ST}} = 0.17$ and $c_{\mathrm{LT}} = 0.083$ with 95% confidence bounds of [0.13, 0.21] and [0.062, 0.104]. We now have

$$\begin{aligned}-\overline{w'b'}_e &= 0.17\frac{u^{*3}}{h_b}(1 + 0.49\mathrm{La}_{\mathrm{SL}}^{-2}) + 0.15\frac{w^{*3}}{h_b}\\ &= \frac{u^{*3}}{h_b}\left(0.17 + 0.083\mathrm{La}_{\mathrm{SL}}^{-2} - 0.15\frac{h_b}{\kappa L}\right). \qquad (21)\end{aligned}$$

Previous studies suggest that the Langmuir-turbulence-induced $\overline{w'b'}_e$ scales with $\mathrm{La}_t^{-2}u^{*3}/h_b$ (e.g., Grant and Belcher 2009; McWilliams et al. 2014). For comparison, fitting the same data with $\mathrm{La}_x = \mathrm{La}_t$ and $p = 2$ is also shown (Fig. 8b).

Figure 9a shows the normalized $\overline{w'b'}_e$ approximated from (21) in the $\mathrm{La}_{\mathrm{SL}}$–$-h_b/(\kappa L)$ regime diagram. Overlaid light gray contours show the typical conditions in a global climate model estimated from daily averaged output in one year of a global fully coupled CESM simulation (PI-WW3 in Li et al. 2017), and white symbols mark all the wave-forced simulations in this study. Langmuir turbulence enhances $\overline{w'b'}_e$ under weak surface destabilizing buoyancy forcing, but has little effect when convection dominates.

Figure 9b illustrates the comparison of $\overline{w'b'}_e$ approximated by (21) versus that simulated in the LES. Note that logarithmic axes are used, so the deviations from the reference line reflect relative errors. The convergence of the scatter onto the reference line at relatively larger values, both in the convective regime (black and gray symbols) and Langmuir regime (colored symbols), suggests that (21) is able to capture the variations of $\overline{w'b'}_e$ under strong convective or Langmuir turbulence conditions. Significant relative errors still exist when both forcings are relatively weak. This is presumably due to processes that are not considered in this study, such as the inertial oscillation. Preliminary simulations suggest some dependence of $\overline{w'b'}_e$ on the Coriolis parameter, especially for the weak Langmuir turbulence cases. Exploration and quantification of the effects of inertial oscillations on $\overline{w'b'}_e$ is the topic of an ongoing study.

---

[5] Note that Fig. 8a suggests $c_{\mathrm{CT}} = 0.14$, which is an estimate with data from S-NL. It resulted in greater error than $c_{\mathrm{CT}} = 0.15$ when data from other subsets are considered.

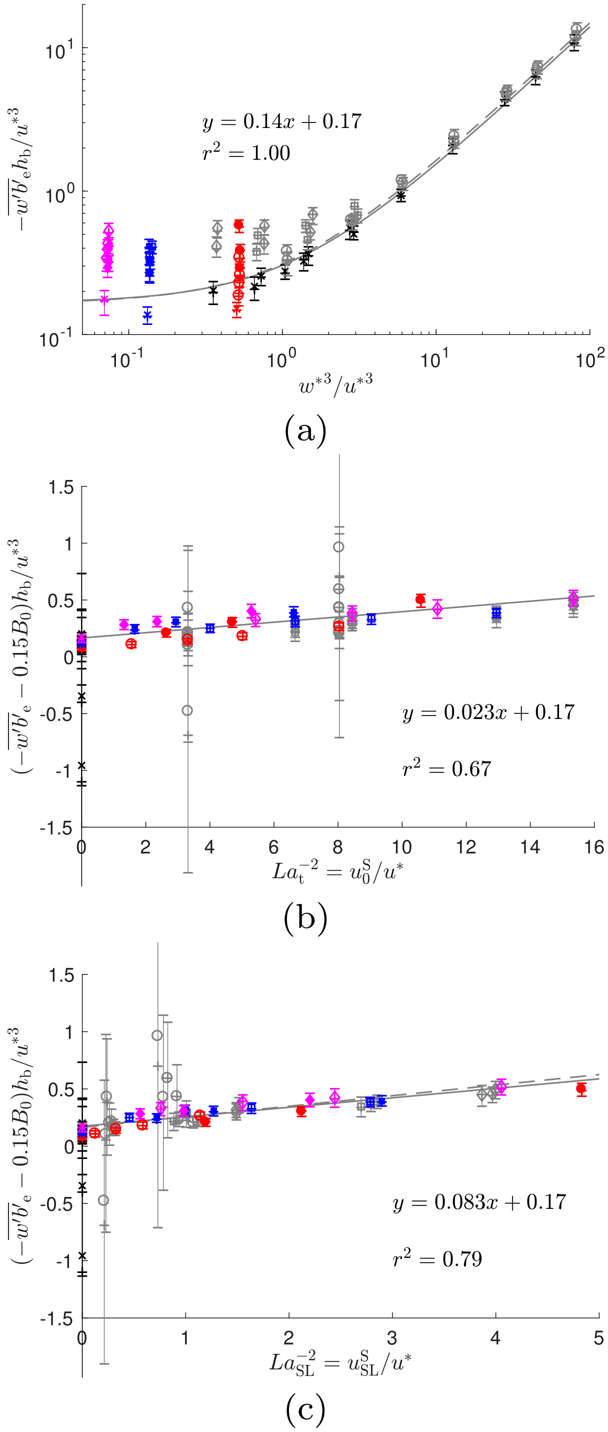

FIG. 8. Scaling the entrainment buoyancy flux: (a) $\overline{w'b'}_e h_b/u^{*3}$ is plotted against $B_0 h_b/u^{*3} = w^{*3}/u^{*3}$. Curve fitting (solid curve) is applied to data from S-NL (crosses). The normalized residual $\overline{w'b'}_e$, with $c_{\mathrm{CT}}B_0$ subtracted, is plotted against (b) $\mathrm{La}_t^{-2} = u_0^S/u^*$ and (c) $\mathrm{La}_{\mathrm{SL}}^{-2} = u_{\mathrm{SL}}^S/u^*$. Curve fitting (solid curve) is applied to data from S-L1 and S-L2 (colored symbols). The dashed curves in (a) and (c) illustrate a least squares regression with all the data. Error bars show the 25th, 50th, and 75th percentiles within an inertial oscillation period. Symbols are as in Fig. 2.

## 5. Entrainment in KPP

In KPP (Large et al. 1994), the turbulent entrainment is implicitly represented by finding the boundary layer depth that satisfies the stability criterion based on a bulk Richardson number. The boundary layer depth $h_b$ is defined as the smallest depth at which the bulk Richardson number,

$$\mathrm{Ri}_b(z) = \frac{|z|[b_r - b(z)]}{|\mathbf{u}_r - \mathbf{u}(z)|^2 + U_t^2(z)}, \qquad (22)$$

reaches a critical value $\mathrm{Ri}_c = 0.3$. The arguments behind this definition are that the boundary layer eddies with reference velocity $\mathbf{u}_r$ and reference buoyancy $b_r$ should be able to penetrate to a depth $h_b$, where their mean kinetic energy relative to the local flow and TKE all convert to the potential energy. The reference velocity $\mathbf{u}_r$ and buoyancy $b_r$ are averaged over the surface layer $z > -\varepsilon h_b$ with $\varepsilon = 0.1$ to avoid the resolution dependency. The velocity scale $U_t(z)$ to account for the impact of unresolved shear, is parameterized by

$$U_t^2(z) = \frac{C_v N(z) w_s(z)|z|}{\mathrm{Ri}_c \kappa^2}\left(\frac{-\beta_T}{c_s \varepsilon}\right)^{1/2}, \qquad (23)$$

with $N(z)$ the local buoyancy frequency, $w_s(z)$ the turbulent velocity scale for scalars, and parameters $C_v = 2.1 - 200\{\max[0, \min(N, 0.002)]\}$, $c_s = 98.96$, and $\beta_T = -0.2$. In the derivation of (23), an empirically determined relation $\overline{w'b'}_e = \beta_T B_0$ for pure convection is used. The dimensionless constants $c_s$ and $\beta_T$ are empirically determined. The symbols used here are consistent with symbols used in Large et al. (1994).

No effect of Langmuir turbulence is accounted for in the above formulation. With the scaling for $\overline{w'b'}_e$ in (21), modifications to (23) to include the effects of Langmuir turbulence are straightforward. Following the arguments in Large et al. (1994, p. 372), a modified version of $U_t^2$ can be derived as follows. Using (9) and (10) of Large et al. (1994) and ignoring the nonlocal transport term, we have

$$\begin{aligned}\overline{w'b'}_e = \overline{w'b'}\big|_{z=-h_m} &= -(K\partial_z b)\big|_{z=-h_m}\\ &= -h_b w_s(-h_m) G(-h_m/h_b) N(-h_m)^2,\end{aligned} \qquad (24)$$

where $K$ is the KPP diffusivity and $G(z/h_b)$ is a shape function. Considering the special case of pure convection with a well-mixed layer of buoyancy and no mean velocity shear, at the boundary layer base, the numerator of (22) becomes $h_b(h_b - h_m)N(-h_b)^2$. Using $G(-h_m/h_b) = (h_b - h_m)^2/h_b^2$ and $N(-h_m) = N(-h_b)/C_v$ [see Large et al. (1994) for more details], we have

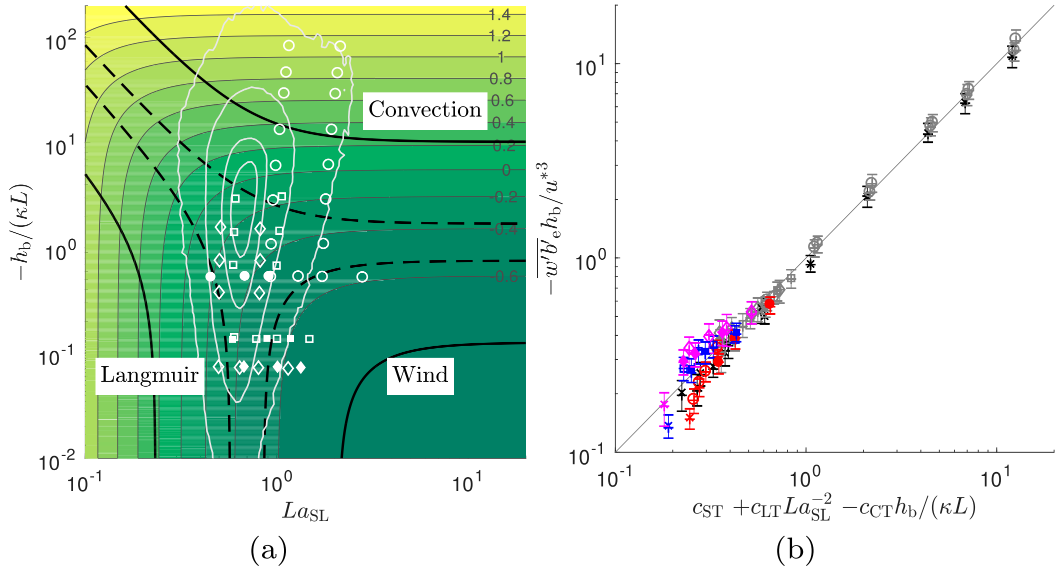

FIG. 9. (a) Regime diagram of the scaled entrainment buoyancy flux, $\log_{10}(-\overline{w'b'}_e h_b/u^{*3})$, plotted as a function of $\mathrm{La}_{SL}$ and $-h_b/(\kappa L)$. The thick solid and dashed lines divide the regime diagram into regions where a single forcing contributes more than 90% and 60%, respectively, of the total $\overline{w'b'}_e$. Overlaid white symbols mark all the wave forced simulations in this study. The light gray contours show the highest 30%, 60%, 90%, and 99% centered distribution of $\mathrm{La}_{SL}$ and $-h_b/(\kappa L)$, estimated from the daily averaged output in one simulated year of a global fully coupled CESM simulation (PI-WW3 in Li et al. 2017). Note that only situations with destabilizing surface buoyancy flux are shown here, which represent about 40% of the total in a simulated year. (b) Comparison between $\overline{w'b'}_e$ predicted by (21) and LES data. Symbols are as in Fig. 2.

$$U_t^2(h_b) = \frac{C_v h_b^2 N(-h_b) N(-h_m)}{\mathrm{Ri}_c}[G(-h_m/h_b)]^{1/2}. \qquad (25)$$

Combining (24), (25), and (21), and noting that $w_s(-h_m) = w_s(-h_b) = w_s(-\varepsilon h_b)$ under unstable conditions, the modified unresolved velocity scale is given by

$$U_{tL}^2(z) = \frac{C_v N(z) w_s(z)|z|}{\mathrm{Ri}_c}\left[\frac{-\overline{w'b'}_e h_b}{w_s(z)^3}\right]^{1/2} = \frac{C_v N(z) w_s(z)|z|}{\mathrm{Ri}_c}\left[\frac{0.15 w^{*3} + 0.17 u^{*3}(1 + 0.49\mathrm{La}_{SL}^{-2})}{w_s(z)^3}\right]^{1/2}. \qquad (26)$$

This is consistent in form with (28) of McWilliams et al. (2014), although here the coefficients are provided based on LES. Note that this scaling should only be applied under destabilizing surface buoyancy flux conditions.

The ratio of (26) to (23) is

$$\frac{U_{tL}^2}{U_t^2} = \left[\frac{0.15 w^{*3} + 0.17 u^{*3}(1 + 0.49\mathrm{La}_{SL}^{-2})}{-\beta_T w_s^3 / c_s \varepsilon \kappa^4}\right]^{1/2}. \qquad (27)$$

In the convective limit, $w_s \rightarrow \kappa(c_s\kappa\varepsilon)^{1/3} w^*$, $U_{tL}^2/U_t^2 \rightarrow (-0.15/\beta_T)^{1/2} \approx 0.87$. In the presence of nonzero $u^*$, the ratio is always slightly greater than this value. So the modifications in (26) make the diagnosed boundary layer depth in KPP slightly shallower in the convective limit. In the weak surface cooling limit, $w_s \rightarrow \kappa u^*$, $U_{tL}^2/U_t^2 \rightarrow 1.83(1 + 0.49\mathrm{La}_{SL}^{-2})^{1/2}$. With $\mathrm{La}_{SL} \approx 0.45$ being the strongest wave forcing explored in this study, this ratio reaches about 3.38. Therefore, in the wind and wave regime, the modified $U_t^2$ will deepen the diagnosed boundary layer depth in KPP.

Figure 10 compares the diagnosed boundary layer depth from different modified versions of KPP[6] to the simulated boundary layer depth in the LES. As already noted in Fig. 1, the traditional KPP (black, labeled LMD96) does a poor job under wave forcing. To account for the effects of Langmuir turbulence on the entrainment, either a Langmuir-number-dependent enhancement factor is applied to $U_t^2$ (RW16) or $u_0^{S2}$ is

---

[6] The boundary layer depth is diagnosed from (22), with the original and modified versions of $U_t^2$, using the mean velocity and buoyancy profiles from LES.

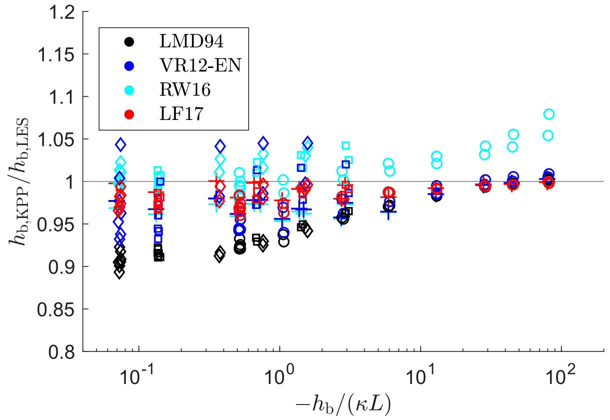

FIG. 10. The ratio of KPP boundary layer depth to $h_b$ in LES. Symbols with different colors represent the estimate from the original KPP (Large et al. 1994) (black), with modifications VR12-EN in Li et al. (2016) (blue), with modifications in RW16 (cyan), and with (26) in this study (red). Here the no-Langmuir cases are marked by plus signs, and the Langmuir cases under 5, 8, and 10 m s$^{-1}$ surface wind forcing are marked by circles, squares, and diamonds, respectively. Note that the black and blue plus signs overlap.

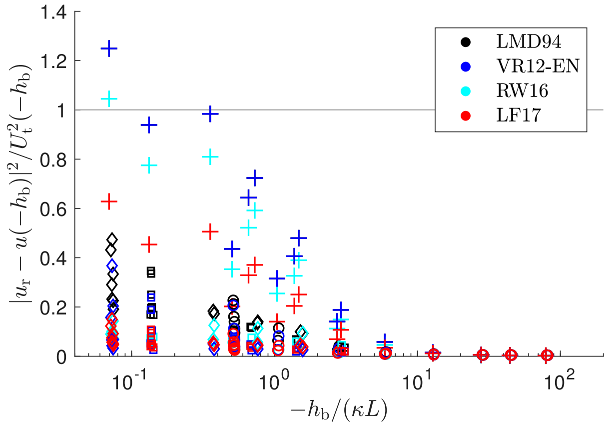

FIG. 11. The ratio of the squared velocity difference at the base of the boundary layer to the squared unresolved velocity scale $|\mathbf{u}_r - \mathbf{u}(-h_b)|^2/U_t^2(-h_b)$ vs $-h_b/(\kappa L)$. Symbols are as in Fig. 10.

added to $U_t^2$ [VR12-EN scheme in Li et al. (2016)]. As shown by the cyan symbols in Fig. 10, the RW16 scheme, which is tuned to fit LES results under tropical cyclone conditions, generally overestimates the boundary layer depth under the moderate wind and wave conditions explored in this study. The increasing deep biases as the convective turbulence regime is approached confirm that the same Langmuir turbulence enhancement factor should not be applied in the convection regime. A more comprehensive set of LES results might be required to connect the parameterization of Langmuir-turbulence-enhanced entrainment in this study to results under strong wind cases in RW16. Although the VR12-EN scheme does not seem to worsen KPP under strong convection conditions, the scatter is significant under strong wave forcing. In the next section, Figs. 12 and 13 demonstrate that the VR12-EN scheme causes too much deepening in the simulated mixed layer depth. Much better agreement with the boundary layer depth in LES is found when $U_t^2$ is modified according to (26), as shown by the red symbols in Fig. 10. This modification to KPP is denoted as LF17 hereafter.

Note that the approach described in this section assumes that all the interesting variations of $\overline{w'b'}_e$ as in (21) are due to unresolved turbulence in KPP. The relative contribution from resolved shear versus unresolved turbulence are examined by calculating the ratio $|\mathbf{u}_r - \mathbf{u}(-h_b)|^2/U_t^2(-h_b)$ for all cases using various versions of $U_t^2$. It is found that this ratio is small (<20%) when either convective or Langmuir turbulence dominates (Fig. 11). This is also confirmed by examining the dependence of $\overline{w'b'}_e$ on $|\mathbf{u}_r - \mathbf{u}(-h_b)|^2$ in our simulations, where no significant relation is found (not shown). Furthermore, from a purely practical perspective, the degree to which a climate model implementing this scheme accurately models shear will be dependent on the climate model vertical resolution, numerics (e.g., Petersen et al. 2015), and representation of Stokes forces (Suzuki and Fox-Kemper 2016). Therefore, this assumption seems to be reasonable at least for the parameter space explored in this study, except for the purely wind-driven cases, which seldom occur in both the climate models and the real ocean. Under strong wind forcing, for example, under tropical cyclone conditions as described in RW16, this assumption is likely to break (see further discussion in section 8).

## 6. Global impact in a climate model

To assess the global impact of the entrainment induced by Langmuir turbulence at the base of the OSBL, the modified KPP with the unresolved velocity scale from (26) is implemented and tested in a global climate model. The CESM-WAVEWATCH III framework described in Li et al. (2016) is used, where a prognostic wave model, WAVEWATCH III (Tolman 2009), is incorporated into the NCAR CESM and coupled with its ocean component. The details of the coupling and sensitivities of global climate variables to the parameterized Langmuir mixing are discussed in Li et al. (2016, 2017).

The simulation setup is essentially the same as the ocean–wave coupled simulations described in Li et al. (2017) and therefore only briefly repeated here. The ocean model is running on a nominal 1°-resolution grid, forced by the interannually varying (62-yr forcing cycle) Coordinated Ocean-Ice Reference Experiments phase II atmospheric datasets (CORE-II; Large and Yeager 2009). The wave model is running on a 3.2° × 4° latitude–longitude grid with 25 frequency and 24 directional bins, forced by the same wind dataset from CORE-II and two-way coupled with the ocean model. All ocean–wave coupled simulations are branched from an ocean-only control simulation (CTRL), which has been integrated for 194 model years to allow the upper ocean to reach equilibrium. The coupled simulations, as well as CTRL, are then integrated for 54 years. The data from the last 50 years of simulations are analyzed here. Because of the almost instantaneous response of the mixed layer depth to the modifications in KPP, this relatively short integration time is enough to show the interesting differences in the mean state at the ocean surface, while remaining within a single CORE-II forcing cycle to avoid the large adjustments associated with the unphysical jump from the end of a forcing cycle to the beginning (Danabasoglu et al. 2014).

For direct comparison, results from two other simulations, corresponding to VR12-MA and VR12-EN in Li et al. (2016), are also shown. Note that VR12-MA implies the same enhancement factor being applied to $U_t^2$ (since it is proportional to $w_s$). The same is true for VR12-EN, with the only difference from VR12-MA being the added $u_0^{S^2}$ in $U_t^2$ to account for the effect of Stokes drift on the entrainment (see further discussion in section 2.2.4 of Li et al. 2016). However, there is no need to apply the same enhancement factor to $w_s$ in (26). Therefore, the enhancement factor affects the vertical diffusivity and viscosity but not $U_t^2$ in LF17. This refinement is performed since the impact of Langmuir turbulence on $\overline{w'b'}_e$ appears to be different than on $\langle\overline{w'^2}\rangle_{h_m}$ (Fig. 7). In addition, to avoid overestimation of $\overline{w'b'}_e$ under misaligned wind and wave conditions, $\mathrm{La}_{\mathrm{SL,proj}}$, instead of $\mathrm{La}_{\mathrm{SL}}$, is used here.[7] This practice is supported by preliminary LES runs with misaligned wind and wave forcing, though a refined scaling law accounting for the effects of wind-wave misalignment is left to future work.

Figures 12 and 13 show the summer and winter mean mixed layer depth in both hemispheres, defined as the depth where the potential density (referenced to surface) changes by 0.03 kg m$^{-3}$ from its surface value. Their zonal means are shown in the Figs. 12b and 13b. The RMS errors in comparison with the observations of de Boyer Montégut et al. (2004), evaluated in different regions, are shown in Table 3. VR12-MA improves the simulated mixed layer depth in the extratropical regions, especially in the Southern Ocean, although significantly shallow biases still exist in summer and at some locations in winter (Figs. 12d, 13d). VR12-EN generally causes too much entrainment, resulting in too deep mixed layer depth throughout the year (Figs. 12e, 13e). These are consistent with Li et al. (2016, 2017). LF17 further improves the simulated summer mean mixed layer depth in the extratropical regions significantly and slightly alleviates the degradation in the tropical region. In winter, the mixed layer depth in LF17 is generally deeper than VR12-MA in the extratropical regions, but with similar RMS errors. Apparent shallow biases can still be found at some locations in the Southern Ocean, and the spatial distribution of the mixed layer depth, for example, in the northern Atlantic and the narrow band of deep mixed layer in the Southern Ocean, are clearly not well simulated.

Enhanced surface vertical mixing in the Southern Ocean, especially in winter, increases the water ventilation even below the mixed layer (see, e.g., Fig. 6 in Li et al. 2016). Comparing with VR12-MA (not shown), LF17 improves the simulated chlorofluorocarbon (CFC) concentration under ~300 m, where the CFC concentration is biased low, but worsens as it nears the surface, introducing high concentration biases there. But the overall RMS errors in CFCs are similar to VR12-MA.

## 7. Summary

This LES-based study has been focusing on assessing the impact of Langmuir turbulence on the entrainment buoyancy flux $\overline{w'b'}_e$ under various idealized wind, wave, and destabilizing surface buoyancy forcing. The main conclusions are summarized as follows:

- No remarkable interactions between Langmuir turbulence and convective turbulence are found in our simulations. The implication for Langmuir turbulence parameterization is that a Langmuir-number-related enhancement factor (e.g., McWilliams and Sullivan 2000; Li et al. 2016) should only be applied on the shear turbulence induced vertical mixing, not on the total that also includes contributions of convective turbulence.
- It appears that $\overline{w'b'}_e$ is not directly controlled by $(\langle\overline{w'^2}\rangle_{h_m})^{1/2}$, which describes the intensity of vertical mixing within the OSBL. Therefore, a separate scaling law for $\overline{w'b'}_e$ is necessary.
- An estimate of $\overline{w'b'}_e$ scaling is given by (21).
- The parameterized unresolved velocity scale in KPP is modified to incorporate the scaling law (21) to account for the effects of Langmuir turbulence on entrainment.
- Implementing the modified KPP in a global climate model appears to improve the simulated mixed layer depth, especially in the Southern Ocean in summer.

---

[7] Parameter $\mathrm{La}_{\mathrm{SL,proj}}$ reduces to $\mathrm{La}_{\mathrm{SL}}$ when wind and waves are aligned, but is generally greater when wind and waves are misaligned.

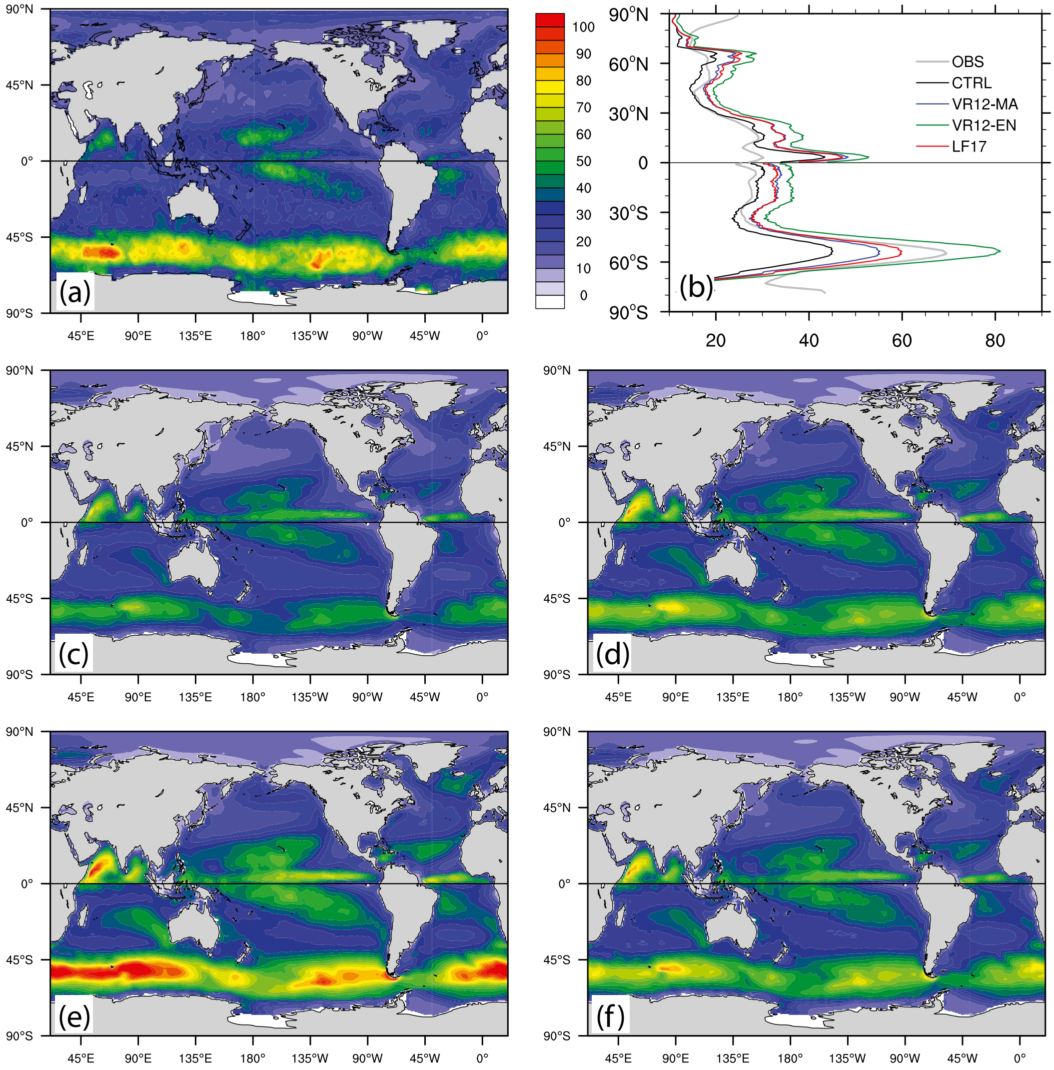

FIG. 12. Impact of Langmuir turbulence on the summer mean mixed layer depth (m) for both hemispheres. (a) Observations from de Boyer Montégut et al. (2004), updated to include the Argo data up through 2012 (Rodgers et al. 2014). (c) The result without Langmuir turbulence (CTRL). (d)–(f) Results with parameterization schemes of VR12-MA, VR12-EN, and this study (LF17), respectively. Mixed layer depths are averaged over July–September (JAS) for the Northern Hemisphere (NH) and January–March (JFM) for the Southern Hemisphere (SH). (b) The zonal mean mixed layer depth for all cases.

## 8. Discussion

This study focuses on the responses of the entrainment buoyancy flux $\overline{w'b'}_e$ in a quasi-equilibrium state under various constant forcing, with a particular interest in parameterizing the effects of Langmuir turbulence in climate models. Therefore, relatively weak wind forcing is adopted in all the simulations. Under strong wind forcing, such as under tropical cyclone conditions, rapid mixed layer deepening due to resonant wind-driven mixing may occur (e.g., Large and Crawford 1995; Crawford and Large 1996; Skyllingstad et al. 2000; RW16). In those cases, the variability of $\overline{w'b'}_e$ should be significantly larger and a greater number of ensemble simulations may be necessary. The effects of Langmuir turbulence on the vertical mixing under strong wind forcing is discussed in, for example, Harcourt and D'Asaro (2008) and RW16.

In addition, with stronger wind forcing, regime transition of the dominating mechanisms that affect $\overline{w'b'}_e$ might be possible, as indicated by, for example, the inconsistencies between the results of this study and that in RW16 in Fig. 10. Here the energy source of entrainment, converting TKE to potential energy, is dominated by the enhanced downward TKE transport in the presence of Langmuir turbulence. However, under strong wind

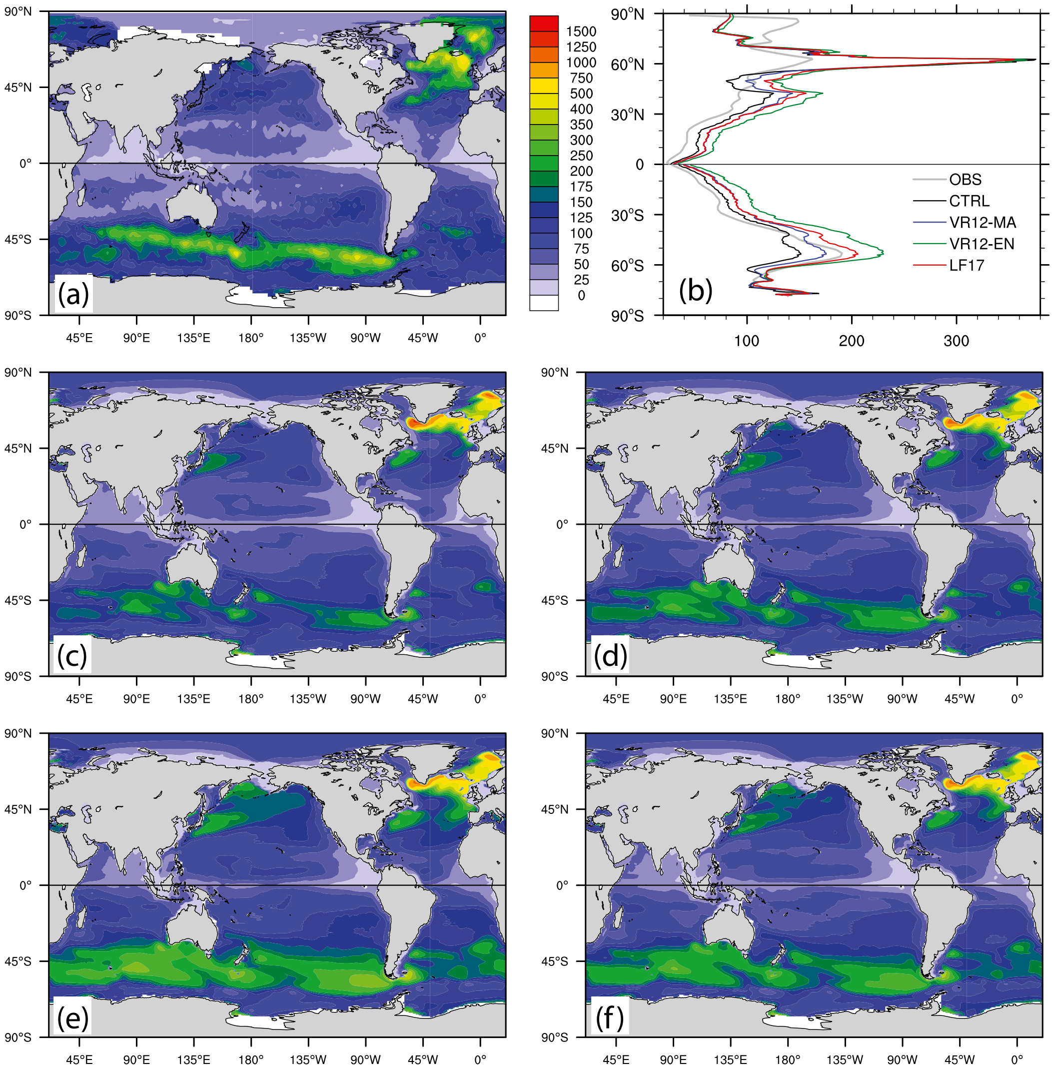

FIG. 13. As in Fig. 12, but for winter mean mixed layer depth averaged over JFM for the NH and JAS for the SH.

forcing, $\overline{w'b'}_e$ is expected to be more affected by the strong shear turbulence locally produced at the base of the OSBL associated with inertial oscillations.

When deriving the modifications to $U_t^2$ in (26) in section 5, it is assumed that all the interesting variations of $\overline{w'b'}_e$ are due to unresolved turbulence in KPP. This assumption may fail and therefore the entrainment may be overestimated in the regime of weak Langmuir turbulence and weak convection, especially when the vertical resolution is high enough to resolve the shear across

TABLE 3. RMS errors (m) of summer and winter mean mixed layer depth in comparison with observation from (de Boyer Montégut et al. 2004), which is updated to include the Argo data up through 2012 (Rodgers et al. 2014). Numbers with ± sign give the 90% confidence interval, estimated from the RMS errors of 1000 bootstrap estimates of the 50-yr mean.

| | Summer | | | Winter | | |
|---|---|---|---|---|---|---|
| Case | Global | South of 30° S | 30° S–30° N | Global | South of 30° S | 30° S–30° N |
| CTRL | 10.28 ± 0.29 | 16.00 ± 0.48 | 6.57 ± 0.23 | 50.24 ± 1.42 | 52.52 ± 0.54 | 15.89 ± 0.33 |
| VR12-MA | 9.31 ± 0.28 | 10.64 ± 0.49 | 9.60 ± 0.33 | 47.65 ± 1.15 | 48.47 ± 0.49 | 22.98 ± 0.42 |
| VR12-EN | 11.65 ± 0.29 | 11.91 ± 0.83 | 12.79 ± 0.39 | 56.85 ± 0.93 | 61.30 ± 1.21 | 33.60 ± 0.55 |
| LF17 | 8.48 ± 0.24 | 8.92 ± 0.39 | 9.15 ± 0.30 | 47.78 ± 1.08 | 49.98 ± 0.77 | 22.43 ± 0.43 |

the boundary layer base. Given the relatively coarse vertical resolution in the ocean climate model (10 m near the surface) and the highly parameterized diurnal cycle (Large and Caron 2015), we do not expect that overestimating the entrainment in that regime will significantly affect the results shown in section 6. Nevertheless, great care should be taken when (26) is applied to other situations.

No effects of misaligned wind and waves are accounted for in the scaling of $\overline{w'b'}_e$ in this study. Langmuir turbulence under swell conditions are studied in Van Roekel et al. (2012) and McWilliams et al. (2014), but the effects of wind-wave misalignment on the Langmuir-turbulence-induced $\overline{w'b'}_e$ are not yet clear. One might expect reduced enhancement due to the suppressed Langmuir turbulence intensity under misaligned wind and waves. A more comprehensive set of LES simulations under various swell conditions might be required to assess this effect quantitatively.

The dependence of the mean vertical velocity variance $\langle\overline{w'^2}\rangle_{h_m}$ on the intensity of Langmuir turbulence, when measured by $\mathrm{La_{SL}}$, generally agrees with previous studies (e.g., Harcourt and D'Asaro 2008; Van Roekel et al. 2012). Interestingly, similar dependence on $\mathrm{La_{SL}}$ appears to remain valid in the presence of convective turbulence, with the contributions from convective turbulence simply being additive. This is somehow expected, as the turbulent motions of convective turbulence are weak in the direction of Stokes shear, which is mostly in the horizontal direction, and thereby the Stokes shear force is weak (Suzuki and Fox-Kemper 2016). Therefore, any dynamically nonlinear interactions between convective turbulence and Langmuir turbulence have no significant bearing on predicting entrainment.

The form of the scaling law for $\overline{w'b'}_e$, (21), is based on arguments on the TKE budget. However, no claim has been made that the contribution from Stokes production scales with $\mathrm{La}_{\mathrm{SL}}^{-2}u^{*3}/h_b = u^{*2}u_{\mathrm{SL}}^S/h_b$. Instead, the contributions of Stokes production and mean shear production are probably not separable, as the mean shear is strongly affected by the presence of Stokes drift due to the anti-Stokes effect (McWilliams and Fox-Kemper 2013; Haney et al. 2015). Scaling the Lagrangian shear production is probably the right way to go, and a more comprehensive measure of the effects of Langmuir turbulence considering the full Stokes drift profile might be required.

This work is among a series of efforts trying to improve KPP to account for the effects of Langmuir turbulence (e.g., McWilliams and Sullivan 2000; Smyth et al. 2002; McWilliams et al. 2014; Li et al. 2016; RW16; Li et al. 2017). When its effects are parameterized in a climate model, improvements in the simulated mixed layer are generally found in the extratropical regions, especially in the Southern Ocean in summer. However, significant biases of the Southern Ocean mixed layer depth in winter still exist, with biases in the spatial distribution in addition to its magnitude. Other approaches lead to similar results (e.g., Noh et al. 2011, 2016). One possible remedy is to better represent the storminess in the climate model by increasing the spatial resolution and coupling frequency (e.g., McClean et al. 2011). Note that under stormy conditions, the scaling of $\overline{w'b'}_e$ proposed here, which generally describes the effects of Langmuir turbulence in low wind cases, is probably not sufficient. Connecting to high wind cases (e.g., RW16) seamlessly is a direction for future work. In addition, improvements in the representation of other physical processes in the ocean models, such as mesoscale and submesoscale eddies (Gent et al. 1995; Fox-Kemper et al. 2011), isopycnal mixing (Redi 1982), and oceanic near-inertial waves (Jochum et al. 2013), are probably also necessary to further reduce those biases.

Finally, it should be noted that the only wave parameter required in the modified $U_t^2$ in (26) is $\mathrm{La_{SL}}$, which is reasonably estimated by the "theory wave" approach described in Li et al. (2017) without the need for a full prognostic wave model (see their Fig. 2f). Therefore, the refinement of KPP developed in this study can be easily combined with the theory wave approach in Li et al. (2017) to provide a computationally efficient, while still reasonable, parameterization for the effects of Langmuir turbulence on both the mixing within the OSBL and the entrainment at the base.

*Acknowledgments.* We appreciate the constructive comments and suggestions from Ramsey Harcourt and two anonymous reviewers. Support from NSF Awards 1258907 and 1350795 to BF-K is gratefully acknowledged. This material is based upon work supported by the National Science Foundation under Grant DMS-1439786 while the author was in residence at the Institute for Computational and Experimental Research in Mathematics in Providence, RI, during the spring 2017 semester. All the LES runs were conducted using computational resources and services at the Center for Computation and Visualization, Brown University, supported in part by the National Science Foundation EPSCoR Cooperative Agreement EPS-1004057. We are grateful to Peter Sullivan for making the LES code available. Simulations with CESM were conducted using the high-performance computing resources and support from Yellowstone (ark:/85065/d7wd3xhc) provided by NCAR's Computational and Information Systems Laboratory, sponsored by the National Science Foundation.

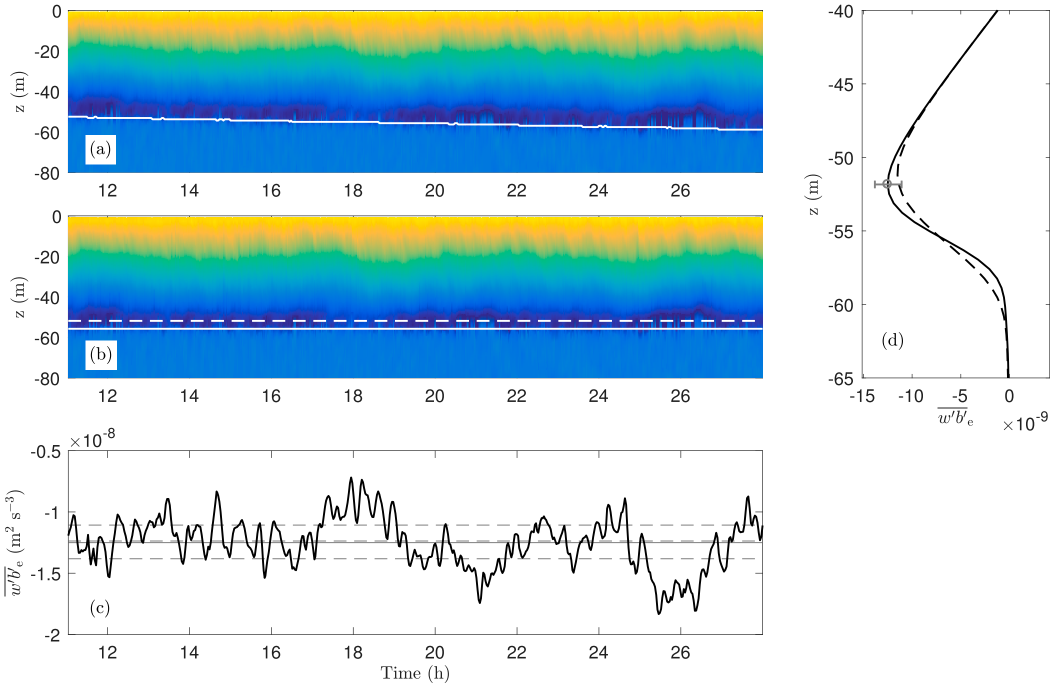

FIG. A1. An example showing the variability of $\overline{w'b'}_e$ within an inertial oscillation period. (a) The original time series of the buoyancy flux profile. White solid curve shows the boundary layer depth $h_b$. (b) As in (a), but adjusted for the deepening of $h_b$. White dashed curve shows the mixed layer depth $h_m$. (c) Time series of $\overline{w'b'}_e$ (black solid curve). The gray solid line shows the mean and the gray dashed lines show the 25th, 50th, and 75th percentiles. (d) The mean buoyancy flux profiles near the base of the boundary layer are shown for the adjusted (solid) and original (dashed) time series. The mean $\overline{w'b'}_e$ is marked by the gray circle, with error bar showing the 25th and 75th percentiles.

## APPENDIX A

### Variability of the Entrainment Buoyancy Flux

Figures A1a and A1b show an example of the time series of $\overline{w'b'}$ profile within an inertial oscillation period, before and after the adjustment for the deepening boundary layer. The time mean $\overline{w'b'}$ profile near the base of the boundary layer for both cases is show in Fig. A1d. Clear differences are seen, with sharper peak of $\overline{w'b'}_e$ after adjustment. In this example, the surface wind is set to $U_{10} = 8\,\mathrm{m\,s^{-1}}$ with fully developed wind waves from the DHH spectrum, and surface cooling of $Q_0 = -100\,\mathrm{W\,m^{-2}}$. For cases with stronger destabilizing forcing, the boundary layer deepens more rapidly and the bias of the mean profile without the adjustment is more significant. The strong variability of $\overline{w'b'}_e$ during an inertial oscillation period is illustrated in Fig. A1c. Overlaid on the time series of $\overline{w'b'}_e$ are its mean, 25th, 50th, and 75th percentiles. Same statistics are also marked by the circle with an error bar in Fig. A1d. Note that the bias of $\overline{w'b'}_e$ without the adjustment for the deepening boundary layer can be significant in comparison with its variability.

## APPENDIX B

### Curve Fitting for the Entrainment Buoyancy Flux

Least squares linear regression is performed using data from all simulations to estimate $c_{\mathrm{ST}}$, $c_{\mathrm{LT}}$, and $c_{\mathrm{CT}}$ in (20), with various $p$ and both $\mathrm{La}_x = \mathrm{La}_t$ and $\mathrm{La}_x = \mathrm{La}_{\mathrm{SL}}$. The results are shown by the blue, red, and black solid curves in Figs. B1a and B1c. The corresponding RMS errors normalized by the mean are shown by the solid curves in Figs. B1b and B1d. The coefficient $c_{\mathrm{CT}} \approx 0.15$ is robust and consistent with previous studies of free convections.

In addition, subsets of data are used to fit the formula in a few limiting cases to constrain the parameters, as well as to ensure robustness of the fitting coefficients. In particular, two subsets of the simulations are tested: S-NL and S-L1 + S-L2, by which the effects of Langmuir turbulence are excluded and emphasized, respectively. Fit to subset S-NL suggests that, as shown in Fig. 8a, $c_{\mathrm{ST}} = 0.17$ and $c_{\mathrm{CT}} = 0.14$. This is consistent with the value $c_{\mathrm{CT}} \approx 0.15$. More importantly, $c_{\mathrm{ST}} = 0.17$ (blue dashed line in Figs. B1a,c) suggests that a possible optimal fit occurs at $p \approx 3$ for $\mathrm{La}_x = \mathrm{La}_t$ and $p \approx 2$ for

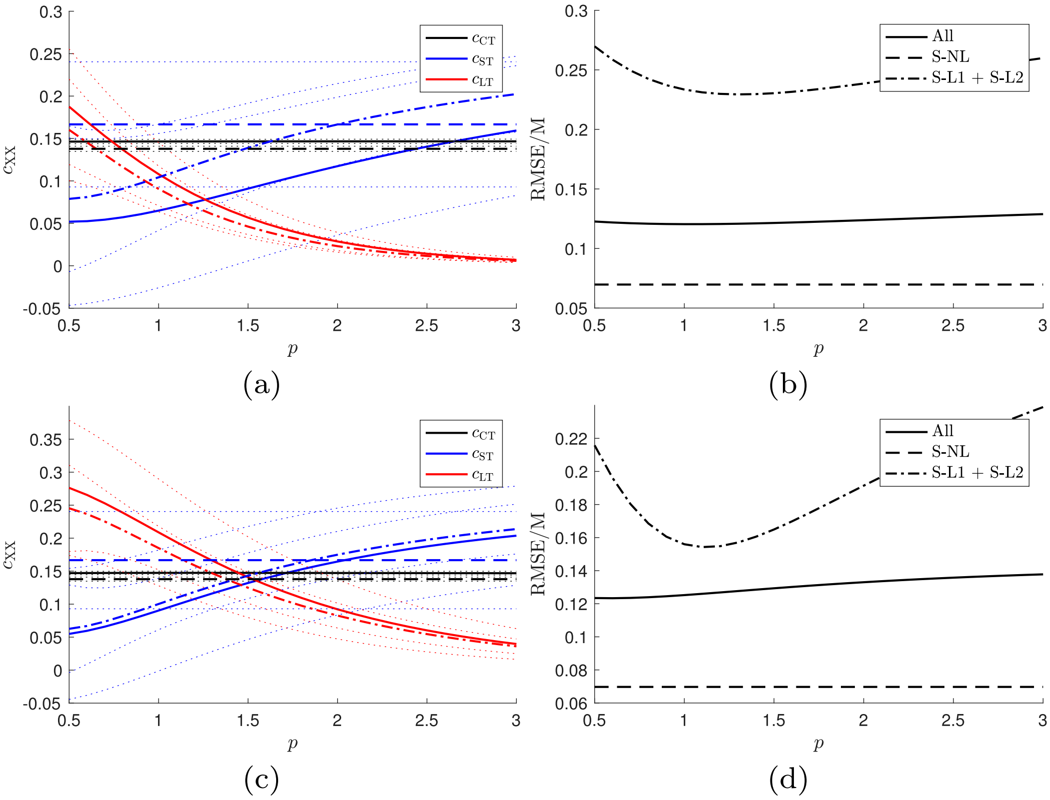

FIG. B1. Curve fitting for $\overline{w'b'}_e$. Estimations of $c_{ST}$, $c_{LT}$, and $c_{CT}$ in (20) by least squares linear regression for various $p$ are shown in black, blue, and red, respectively, with (a) $\mathrm{La}_x = \mathrm{La}_t$ and (c) $\mathrm{La}_x = \mathrm{La}_{SL}$. The corresponding RMS errors normalized by the mean are given in (b) and (d). Solid curves show results with all the data. Dashed and dashed–dotted curves show results with data from the subset S-NL and S-L1 + S-L2, respectively. Dotted curves show the 95% confidence bounds.

$\mathrm{La}_x = \mathrm{La}_{SL}$. Fitting to subset S-L1 + S-L2 with $c_{CT} = 0.15$ ($c_{CT} = 0.14$ was also tested but resulted in greater error) shows consistent estimates of $c_{ST}$ with previous ones if $\mathrm{La}_x = \mathrm{La}_{SL}$ (blue dash–dotted curve in Fig. B1c), but not if $\mathrm{La}_x = \mathrm{La}_t$ (blue dash–dotted curve in Fig. B1a). Therefore, $\mathrm{La}_x = \mathrm{La}_{SL}$ and $p = 2$ are chosen, and $c_{ST} = 0.17$ and $c_{LT} = 0.083$ are estimated with 95% confidence bounds of [0.13, 0.21] and [0.062, 0.104].

Note that given $p = 2$, fitting (20) using data from all the simulations gives $c_{ST} = 0.16$, $c_{LT} = 0.092$, and $c_{CT} = 0.147$, with 95% confidence bounds of [0.084, 0.246], [0.047, 0.137], and [0.144, 0.150]. A comparison is shown in Fig. 8 by the dashed curves, which is almost indistinguishable from the solid curves.

## REFERENCES

Belcher, S. E., and Coauthors, 2012: A global perspective onLangmuir turbulence in the ocean surface boundary layer. *Geophys. Res. Lett.*, **39**, L18605, https://doi.org/10.1029/2012GL052932.

Breivik, Ø., P. A. E. M. Janssen, and J.-R. Bidlot, 2014: Approximate Stokes drift profiles in deep water. *J. Phys. Oceanogr.*, **44**, 2433–2445, https://doi.org/10.1175/JPO-D-14-0020.1.

——, J.-R. Bidlot, and P. A. E. M. Janssen, 2016: A Stokes drift approximation based on the Phillips spectrum. *Ocean Modell.*, **100**, 49–56, https://doi.org/10.1016/j.ocemod.2016.01.005.

Craik, A. D. D., and S. Leibovich, 1976: A rational model for Langmuir circulations. *J. Fluid Mech.*, **73**, 401–426, https://doi.org/10.1017/S0022112076001420.

Crawford, G. B., and W. G. Large, 1996: A numerical investigation of resonant inertial response of the ocean to wind forcing. *J. Phys. Oceanogr.*, **26**, 873–891, https://doi.org/10.1175/1520-0485(1996)026<0873:ANIORI>2.0.CO;2.

Danabasoglu, G., and Coauthors, 2014: North Atlantic simulations in Coordinated Ocean-Ice Reference Experiments phase II (CORE-II). Part I: Mean states. *Ocean Modell.*, **73**, 76–107, https://doi.org/10.1016/j.ocemod.2013.10.005.

D'Asaro, E. A., 2001: Turbulent vertical kinetic energy in the ocean mixed layer. *J. Phys. Oceanogr.*, **31**, 3530–3537, https://doi.org/10.1175/1520-0485(2002)031<3530:TVKEIT>2.0.CO;2.

——, 2014: Turbulence in the upper-ocean mixed layer. *Annu. Rev. Mar. Sci.*, **6**, 101–115, https://doi.org/10.1146/annurev-marine-010213-135138.

——, J. Thomson, A. Y. Shcherbina, R. R. Harcourt, M. F. Cronin, M. A. Hemer, and B. Fox-Kemper, 2014: Quantifying upper ocean turbulence driven by surface waves. *Geophys. Res. Lett.*, **41**, 102–107, https://doi.org/10.1002/2013GL058193.

de Boyer Montégut, C., C. Madec, A. S. Fischer, A. Lazar, and D. Iudicone, 2004: Mixed layer depth over the global ocean: An examination of profile data and a profile-based climatology. *J. Geophys. Res.*, **109**, C12003, https://doi.org/10.1029/2004JC002378.

Donelan, M. A., J. Hamilton, and W. H. Hui, 1985: Directional spectra of wind-generated waves. *Philos. Trans. Roy. Soc. London*, **A315**, 509–562, https://doi.org/10.1098/rsta.1985.0054.

Fox-Kemper, B., and Coauthors, 2011: Parameterization of mixed layer eddies. III: Implementation and impact in global ocean climate simulations. *Ocean Modell.*, **39**, 61–78, https://doi.org/10.1016/j.ocemod.2010.09.002.

Gent, P. R., J. Willebrand, T. J. McDougall, and J. C. McWilliams, 1995: Parameterizing eddy-induced tracer transports in ocean circulation models. *J. Phys. Oceanogr.*, **25**, 463–474, https://doi.org/10.1175/1520-0485(1995)025<0463:PEITTI>2.0.CO;2.

Grant, A. L. M., and S. E. Belcher, 2009: Characteristics of Langmuir turbulence in the ocean mixed layer. *J. Phys. Oceanogr.*, **39**, 1871–1887, https://doi.org/10.1175/2009JPO4119.1.

——, and ——, 2011: Wind-driven mixing below the oceanic mixed layer. *J. Phys. Oceanogr.*, **41**, 1556–1575, https://doi.org/10.1175/JPO-D-10-05020.1.

Hamlington, P. E., L. P. Van Roekel, B. Fox-Kemper, K. Julien, and G. P. Chini, 2014: Langmuir–submesoscale interactions: Descriptive analysis of multiscale frontal spindown simulations. *J. Phys. Oceanogr.*, **44**, 2249–2272, https://doi.org/10.1175/JPO-D-13-0139.1.

Haney, S., B. Fox-Kemper, K. Julien, and A. Webb, 2015: Symmetric and geostrophic instabilities in the wave-forced ocean mixed layer. *J. Phys. Oceanogr.*, **45**, 3033–3056, https://doi.org/10.1175/JPO-D-15-0044.1.

Harcourt, R. R., and E. A. D'Asaro, 2008: Large-eddy simulation of Langmuir turbulence in pure wind seas. *J. Phys. Oceanogr.*, **38**, 1542–1562, https://doi.org/10.1175/2007JPO3842.1.

Jochum, M., B. P. Briegleb, G. Danabasoglu, W. G. Large, N. J. Norton, S. R. Jayne, M. H. Alford, and F. O. Bryan, 2013: The impact of oceanic near-inertial waves on climate. *J. Climate*, **26**, 2833–2844, https://doi.org/10.1175/JCLI-D-12-00181.1.

Kenyon, K. E., 1969: Stokes drift for random gravity waves. *J. Geophys. Res.*, **74**, 6991–6994, https://doi.org/10.1029/JC074i028p06991.

Kukulka, T., A. J. Plueddemann, J. H. Trowbridge, and P. P. Sullivan, 2009: Significance of Langmuir circulation in upper ocean mixing: Comparison of observations and simulations. *Geophys. Res. Lett.*, **36**, L10603, https://doi.org/10.1029/2009GL037620.

——, ——, ——, and ——, 2010: Rapid mixed layer deepening by the combination of Langmuir and shear instabilities: A case study. *J. Phys. Oceanogr.*, **40**, 2381–2400, https://doi.org/10.1175/2010JPO4403.1.

Large, W. G., and S. Pond, 1981: Open ocean momentum flux measurements in moderate to strong winds. *J. Phys. Oceanogr.*, **11**, 324–336, https://doi.org/10.1175/1520-0485(1981)011<0324:OOMFMI>2.0.CO;2.

——, and G. B. Crawford, 1995: Observations and simulations of upper-ocean response to wind events during the Ocean Storms Experiment. *J. Phys. Oceanogr.*, **25**, 2831–2852, https://doi.org/10.1175/1520-0485(1995)025<2831:OASOUO>2.0.CO;2.

——, and S. G. Yeager, 2009: The global climatology of an interannually varying air–sea flux data set. *Climate Dyn.*, **33**, 341–364, https://doi.org/10.1007/s00382-008-0441-3.

——, and J. M. Caron, 2015: Diurnal cycling of sea surface temperature, salinity, and current in the CESM coupled climate model. *J. Geophys. Res. Oceans*, **120**, 3711–3729, https://doi.org/10.1002/2014JC010691.

——, J. C. McWilliams, and S. C. Doney, 1994: Oceanic vertical mixing: A review and a model with a nonlocal boundary layer parameterization. *Rev. Geophys.*, **32**, 363–403, https://doi.org/10.1029/94RG01872.

Leibovich, S., 1980: On wave-current interaction theories of Langmuir circulations. *J. Fluid Mech.*, **99**, 715–724, https://doi.org/10.1017/S0022112080000857.

Lenain, L., and W. K. Melville, 2017: Measurements of the directional spectrum across the equilibrium saturation ranges of wind-generated surface waves. *J. Phys. Oceanogr.*, **47**, 2123–2138, https://doi.org/10.1175/JPO-D-17-0017.1.

Li, M., and C. Garrett, 1997: Mixed layer deepening due to Langmuir circulation. *J. Phys. Oceanogr.*, **27**, 121–132, https://doi.org/10.1175/1520-0485(1997)027<0121:MLDDTL>2.0.CO;2.

——, ——, and E. D. Skyllingstad, 2005: A regime diagram for classifying turbulent large eddies in the upper ocean. *Deep-Sea Res. I*, **52**, 259–278, https://doi.org/10.1016/j.dsr.2004.09.004.

Li, Q., A. Webb, B. Fox-Kemper, A. Craig, G. Danabasoglu, W. G. Large, and M. Vertenstein, 2016: Langmuir mixing effects on global climate: WAVEWATCH III in CESM. *Ocean Modell.*, **103**, 145–160, https://doi.org/10.1016/j.ocemod.2015.07.020.

——, B. Fox-Kemper, Ø. Breivik, and A. Webb, 2017: Statistical models of global Langmuir mixing. *Ocean Modell.*, **113**, 95–114, https://doi.org/10.1016/j.ocemod.2017.03.016.

McClean, J. L., and Coauthors, 2011: A prototype two-decade fully-coupled fine-resolution CCSM simulation. *Ocean Modell.*, **39**, 10–30, https://doi.org/10.1016/j.ocemod.2011.02.011.

McWilliams, J. C., and P. P. Sullivan, 2000: Vertical mixing by Langmuir circulations. *Spill Sci. Technol. Bull.*, **6**, 225–237, https://doi.org/10.1016/S1353-2561(01)00041-X.

——, and B. Fox-Kemper, 2013: Oceanic wave-balanced surface fronts and filaments. *J. Fluid Mech.*, **730**, 464–490, https://doi.org/10.1017/jfm.2013.348.

——, P. P. Sullivan, and C.-H. Moeng, 1997: Langmuir turbulence in the ocean. *J. Fluid Mech.*, **334**, 1–30, https://doi.org/10.1017/S0022112096004375.

——, E. Huckle, J.-H. Liang, and P. P. Sullivan, 2014: Langmuir turbulence in swell. *J. Phys. Oceanogr.*, **44**, 870–890, https://doi.org/10.1175/JPO-D-13-0122.1.

Moeng, C.-H., 1984: A large-eddy-simulation model for the study of planetary boundary-layer turbulence. *J. Atmos. Sci.*, **41**, 2052–2062, https://doi.org/10.1175/1520-0469(1984)041<2052:ALESMF>2.0.CO;2.

——, and P. P. Sullivan, 1994: A comparison of shear- and buoyancy-driven planetary boundary layer flows. *J. Atmos. Sci.*, **51**, 999–1022, https://doi.org/10.1175/1520-0469(1994)051<0999:ACOSAB>2.0.CO;2.

Niiler, P., and E. Kraus, 1977: One-dimensional models of the upper ocean. *Modelling and Prediction of the Upper Layers of the Ocean*, E. Kraus, Ed., Pergamon, 143–172.

Noh, Y., G. Goh, and S. Raasch, 2011: Influence of Langmuir circulation on the deepening of the wind-mixed layer. *J. Phys. Oceanogr.*, **41**, 472–484, https://doi.org/10.1175/2010JPO4494.1.

——, H. Ok, E. Lee, T. Toyoda, and N. Hirose, 2016: Parameterization of Langmuir circulation in the ocean mixed layer model using LES and its application to the OGCM. *J. Phys. Oceanogr.*, **46**, 57–78, https://doi.org/10.1175/JPO-D-14-0137.1.

Pearson, B., 2014: Langmuir turbulence in the ocean surface boundary layer. Ph.D. thesis, University of Reading, 174 pp.

Petersen, M. R., D. W. Jacobsen, T. D. Ringler, M. W. Hecht, and M. E. Maltrud, 2015: Evaluation of the arbitrary Lagrangian–Eulerian vertical coordinate method in the MPAS-Ocean model. *Ocean Modell.*, **86**, 93–113, https://doi.org/10.1016/j.ocemod.2014.12.004.

Polton, J. A., and S. E. Belcher, 2007: Langmuir turbulence and deeply penetrating jets in an unstratified mixed layer. *J. Geophys. Res.*, **112**, C09020, https://doi.org/10.1029/2007JC004205.

——, D. M. Lewis, and S. E. Belcher, 2005: The role of wave-induced Coriolis–Stokes forcing on the wind-driven mixed layer. *J. Phys. Oceanogr.*, **35**, 444–457, https://doi.org/10.1175/JPO2701.1.

——, J. A. Smith, J. A. MacKinnon, and A. E. Tejada-Martínez, 2008: Rapid generation of high-frequency internal waves beneath a wind and wave forced oceanic surface mixed layer. *Geophys. Res. Lett.*, **35**, L13602, https://doi.org/10.1029/2008GL033856.

Price, J. F., R. A. Weller, and R. Pinkel, 1986: Diurnal cycling: Observations and models of the upper ocean response to diurnal heating, cooling, and wind mixing. *J. Geophys. Res.*, **91**, 8411–8427, https://doi.org/10.1029/JC091iC07p08411.

Redi, M. H., 1982: Oceanic isopycnal mixing by coordinate rotation. *J. Phys. Oceanogr.*, **12**, 1154–1158, https://doi.org/10.1175/1520-0485(1982)012<1154:OIMBCR>2.0.CO;2.

Reichl, B. G., D. Wang, T. Hara, I. Ginis, and T. Kukulka, 2016: Langmuir turbulence parameterization in tropical cyclone conditions. *J. Phys. Oceanogr.*, **46**, 863–886, https://doi.org/10.1175/JPO-D-15-0106.1.

Rodgers, K. B., and Coauthors, 2014: Strong sensitivity of Southern Ocean carbon uptake and nutrient cycling to wind stirring. *Biogeosciences*, **11**, 4077–4098, https://doi.org/10.5194/bg-11-4077-2014.

Skyllingstad, E. D., and D. W. Denbo, 1995: An ocean large-eddy simulation of Langmuir circulations and convection in the surface mixed layer. *J. Geophys. Res.*, **100**, 8501–8522, https://doi.org/10.1029/94JC03202.

——, W. D. Smyth, and G. B. Crawford, 2000: Resonant wind-driven mixing in the ocean boundary layer. *J. Phys. Oceanogr.*, **30**, 1866–1890, https://doi.org/10.1175/1520-0485(2000)030<1866:RWDMIT>2.0.CO;2.

Smith, J. A., 1998: Evolution of Langmuir circulation during a storm. *J. Geophys. Res.*, **103**, 12 649–12 668, https://doi.org/10.1029/97JC03611.

Smith, K. M., P. E. Hamlington, and B. Fox-Kemper, 2016: Effects of submesoscale turbulence on ocean tracers. *J. Geophys. Res. Oceans*, **121**, 908–933, https://doi.org/10.1002/2015JC011089.

Smyth, W. D., and J. N. Moum, 2000: Length scales of turbulence in stably stratified mixing layers. *Phys. Fluids*, **12**, 1327–1342, https://doi.org/10.1063/1.870385.

——, E. D. Skyllingstad, G. B. Crawford, and H. Wijesekera, 2002: Nonlocal fluxes and Stokes drift effects in the K-profile parameterization. *Ocean Dyn.*, **52**, 104–115, https://doi.org/10.1007/s10236-002-0012-9.

Sullivan, P. P., J. C. McWilliams, and W. K. Melville, 2007: Surface gravity wave effects in the oceanic boundary layer: Large-eddy simulation with vortex force and stochastic breakers. *J. Fluid Mech.*, **593**, 405–452, https://doi.org/10.1017/S002211200700897X.

Sutherland, G., G. Reverdin, L. Marié, and B. Ward, 2014: Mixed and mixing layer depths in the ocean surface boundary layer under conditions of diurnal stratification. *Geophys. Res. Lett.*, **41**, 8469–8476, https://doi.org/10.1002/2014GL061939.

Suzuki, N., and B. Fox-Kemper, 2016: Understanding Stokes forces in the wave-averaged equations. *J. Geophys. Res. Oceans*, **121**, 3579–3596, https://doi.org/10.1002/2015JC011566.

——, ——, P. E. Hamlington, and L. P. Van Roekel, 2016: Surface waves affect frontogenesis. *J. Geophys. Res. Oceans*, **121**, 3597–3624, https://doi.org/10.1002/2015JC011563.

Teixeira, M. A. C., 2011: A linear model for the structure of turbulence beneath surface water waves. *Ocean Modell.*, **36**, 149–162, https://doi.org/10.1016/j.ocemod.2010.10.007.

——, and S. E. Belcher, 2002: On the distortion of turbulence by a progressive surface wave. *J. Fluid Mech.*, **458**, https://doi.org/10.1017/S0022112002007838.

——, and ——, 2010: On the structure of Langmuir turbulence. *Ocean Modell.*, **31**, 105–119, https://doi.org/10.1016/j.ocemod.2009.10.007.

Tennekes, H., 1973: A model for the dynamics of the inversion above a convective boundary layer. *J. Atmos. Sci.*, **30**, 558–567, https://doi.org/10.1175/1520-0469(1973)030<0558:AMFTDO>2.0.CO;2.

Thorpe, S. A., T. R. Osborn, D. M. Farmer, and S. Vagle, 2003: Bubble clouds and Langmuir circulation: Observations and models. *J. Phys. Oceanogr.*, **33**, 2013–2031, https://doi.org/10.1175/1520-0485(2003)033<2013:BCALCO>2.0.CO;2.

Tolman, H. L., 2009: User manual and system documentation of WAVEWATCH III version 3.14. MMAB Rep. 276, NOAA/NWS/NCEP/MMAB, 220 pp., http://polar.ncep.noaa.gov/mmab/papers/tn276/MMAB_276.pdf.

Tseng, R.-S., and E. A. D'Asaro, 2004: Measurements of turbulent vertical kinetic energy in the ocean mixed layer from Lagrangian floats. *J. Phys. Oceanogr.*, **34**, 1984–1990, https://doi.org/10.1175/1520-0485(2004)034<1984:MOTVKE>2.0.CO;2.

Van Roekel, L., B. Fox-Kemper, P. P. Sullivan, P. E. Hamlington, and S. R. Haney, 2012: The form and orientation of Langmuir cells for misaligned winds and waves. *J. Geophys. Res.*, **117**, C05001, https://doi.org/10.1029/2011JC007516.

Webb, A., and B. Fox-Kemper, 2011: Wave spectral moments and Stokes drift estimation. *Ocean Modell.*, **40**, 273–288, https://doi.org/10.1016/j.ocemod.2011.08.007.

——, and ——, 2015: Impacts of wave spreading and multidirectional waves on estimating stokes drift. *Ocean Modell.*, **96**, 49–64, https://doi.org/10.1016/j.ocemod.2014.12.007.

Weller, R. A., and J. F. Price, 1988: Langmuir circulation within the oceanic mixed layer. *Deep-Sea Res.*, **35A**, 711–747, https://doi.org/10.1016/0198-0149(88)90027-1.

Wunsch, C., and R. Ferrari, 2004: Vertical mixing, energy, and the general circulation of the oceans. *Annu. Rev. Fluid Mech.*, **36**, 281–314, https://doi.org/10.1146/annurev.fluid.36.050802.122121.